J. Fluid Mech. (2020), *vol*. 900, A18. © The Author(s), 2020.
Published by Cambridge University Press
doi:10.1017/jfm.2020.452

Direct numerical simulation of turbulent flow through a ribbed square duct

S. V. Mahmoodi-Jezeh[1] **and Bing-Chen Wang**[1],†

[1]Department of Mechanical Engineering, University of Manitoba, Winnipeg, MB R3T 5V6, Canada

(Received 16 November 2019; revised 20 March 2020; accepted 31 May 2020)

In this research turbulent flow in a ribbed square duct of different blockage ratios ($Br = 0.05$, 0.1 and 0.2) at a fixed Reynolds number of $Re_b = 5600$ is studied using direct numerical simulation. The results are compared with those of a smooth duct flow. In contrast to the classical two-dimensional rib-roughened boundary-layer flow over a flat plate, the turbulence field is influenced by not only the rib elements but also the four duct sidewalls. The results detail out the three-dimensional effects of the sidewalls and ribs on flow statistics and structures. This study also aims at investigating the effect of blockage ratio on local non-equilibrium of turbulence, large- and small-scale flow anisotropy, and transport of turbulence kinetic energy. It is observed that as the rib height increases, the pressure near the windward face of the rib increases significantly, associated with an accelerated streamwise flow in the duct. Furthermore, an augmentation of the blockage ratio concurrently generates stronger turbulent secondary flow motions, resulting in larger magnitudes of Reynolds stresses near the rib crest. The secondary flow motions drastically alter the turbulent transport processes between the sidewall and duct centre, giving rise to high degrees of non-equilibrium states. The dynamics of coherent structures are studied by examining characteristics of the instantaneous velocity field, swirling strength, temporal auto-correlations, spatial two-point auto-correlations and velocity spectra. The results show that an increase of rib height significantly promotes the ejection and sweep events, which subsequently amplify the strength of vortical motions near the rib crest.

Key words: turbulence simulation, shear layer turbulence, turbulent convection

1. Introduction

Physical interpretation of the complex turbulent flow confined within a ribbed duct has many important engineering applications, such as heat exchangers (Yaglom & Kader 1974; Shishkina & Wagner 2011) and internal turbine blade cooling (Casarsa & Arts 2005; Wang & Sundén 2005; Lohász, Rambaud & Benocci 2006; Wang, Hejcik & Sunden 2007; Han, Dutta & Ekkad 2012; Labbé 2013; Borello, Salvagni & Hanjalić 2015). For the study of ribbed square duct flow with an application to turbine blade cooling, the height of the ribs may vary considerably, and the blockage ratio can go as high as $Br = 0.3$ (Casarsa & Arts 2005; Lohász *et al.* 2006; Labbé 2013). The ribbed square duct flow under investigation is bounded peripherally by one ribbed wall and three smooth walls. It is significantly different from the conventional two-dimensional (2-D) rough-wall

† Email address for correspondence: bingchen.wang@umanitoba.ca

boundary-layer flows in the sense that it is not only highly disturbed by the ribs but also dominated by strong secondary flows in the cross-stream directions of the duct. As a result, a ribbed square duct flow is intrinsically three-dimensional (3-D) and is statistically inhomogeneous in all three directions.

1.1. *Conventional 2-D riblet flow*

In the current literature, studies of 2-D turbulent boundary-layer flows over rough walls are relatively abundant. For instance, Krogstad & Antonia (1994) studied the effects of k-type rough walls on large-scale structures of a turbulent boundary layer using X-wires in a wind tunnel. They found that turbulence structures were profoundly influenced in the outer region by the transverse ribs. Wang, Salewski & Sundén (2010) measured 2-D riblet flows using particle image velocimetry (PIV), and the rib height was up to 20 % of their channel. There are many reported direct numerical simulation (DNS) studies of 2-D riblet flows, well represented by the works of Choi, Moin & Kim (1993), Bhaganagar, Kim & Coleman (2004), Leonardi *et al.* (2004), Orlandi, Lenoardi & Antonia (2006), Ikeda & Durbin (2007), Burattini *et al.* (2008), Liu, Ke & Sung (2008), and Chan *et al.* (2015). For instance, Leonardi *et al.* (2004) conducted DNS of a fully developed 2-D turbulent channel flow with square bars mounted on the bottom wall. They showed that the coherency of streaky structures decreased in the streamwise direction with an increasing pitch-to-height ratio P/H, as a result of intense ejections of fluid from cavities. Here, P and H denote the streamwise rib separation and the rib height, respectively.

According to Perry, Schofield & Joubert (1969) and Bandyopadhyay (1987), the type of roughness switches from the k- to d-type when the pitch-to-height ratio becomes less than three (i.e. $P/H \leq 3$). For the k-type roughness, unstable vortices generated by the ribs and shed upwards to form roughness sublayer structures (Shafi & Antonia 1997). Conversely, for the d-type roughness, stable vortices recirculate within cavities between two nearby ribs. These prototypical physical features have been clearly visualized by Bandyopadhyay (1987) who conducted experiments to investigate the effects of surface roughness on the vortex-shedding pattern in a low-speed wind tunnel, and by Leonardi *et al.* (2003) who studied turbulent boundary-layer flow developed over a plate roughened with transverse ribs using DNS. The classical works reviewed here (e.g. Perry *et al.* 1969; Bandyopadhyay 1987) were conducted primarily based on the 2-D rib-roughened boundary layers. If we follow the convention of these classical papers, the present work would deal only with k-type riblet roughness mounted on the bottom wall of a square duct. However, strictly speaking, the classical definitions of k- or d-type roughnesses established based on the 2-D boundary layers are not entirely applicable to the current 3-D flow, and it would be of interest to investigate the riblet effect on the turbulent flow pattern confined peripherally within a duct.

1.2. *Three-dimensional smooth and ribbed duct flows*

In contrast to 2-D ribbed flows briefly reviewed above, the flow inside a ribbed duct is inhomogeneous in all directions, influenced by not only the ribs but also the confinement of four sidewalls of the square duct. In a smooth square duct, mean and turbulent secondary flow structures appear in the cross-stream directions. Gavrilakis (1992) investigated the mechanism leading to secondary flow generation through the analysis of the transport of mean streamwise vorticity in a smooth square duct at a Reynolds number of $Re_b = DU_b/\nu = 4410$ (based on the duct width D and bulk mean velocity U_b). Following this study, Mompean *et al.* (1996) performed Reynolds-averaged Navier–Stokes (RANS)

simulations using a nonlinear $k-\varepsilon$ model. Their approach was capable of modelling mean secondary flows observed in the DNS study of Gavrilakis (1992). Recently, Pirozzoli *et al.* (2018) conducted a DNS study of a fully developed turbulent flow in a smooth square duct with a wide range of Reynolds numbers, and observed that the mean flow characteristics (such as local skin friction coefficient) were insensitive to the secondary flows. Similar to the flow pattern in a smooth duct briefly reviewed above, dominant secondary flows also occur in the cross-stream directions in a ribbed duct. This is evidenced by the studies of Casarsa & Arts (2005) and Lohász *et al.* (2006), who investigated ribbed duct flows using PIV and large-eddy simulation (LES), respectively. Since the generation of secondary flow motions is strongly associated with the anisotropy of turbulent stresses, it is expected that the strength and the pattern of secondary flows are noticeably altered in a transversely rib-roughened duct due to the disturbances from the ribs. Hirota, Yokosawa & Fujita (1992) measured fully developed turbulent flows in square and rectangular ducts with perpendicular ribs mounted on one wall using a hot-wire anemometer. They showed that the secondary flow appeared as a large streamwise-elongated vortex adjacent to each vertical sidewall, which transports high momentum fluid from the duct centre towards the duct corner. To study the effect of secondary flow on the statistics of the velocity and temperature fields, Yokosawa *et al.* (1989) measured the mean velocities and Reynolds stresses in a square duct with the bottom and top walls roughened by transverse ribs and compared their results against measurements taken in a smooth square duct. They showed that in comparison with the smooth duct, owing to the presence of ribs and strong secondary flows, the spatial distribution of turbulent shear stress is significantly altered in the rib-roughened duct. Liou, Wu & Chang (1993) conducted laser-Doppler velocimeter (LDV) measurements of a fully developed duct flow with square ribs mounted on the bottom and top walls. They observed that due to the appearance of the mean secondary flow, the impingement region close to the vertical sidewalls resulted in high heat transfer rates. This research finding of Liou *et al.* (1993) was later confirmed by Sewall *et al.* (2006) and Labbé (2013) using LES. Sewall *et al.* (2006) also concluded that both the skin friction and form drags were less sensitive to the secondary flow than the heat transfer coefficient on the ribbed wall. Coletti, Cresci & Arts (2013) measured the turbulent flow confined in a rectangular duct using PIV. In their experiment, transverse square ribs were mounted on the bottom wall of the duct with a blockage ratio of $Br = 0.1$. Besides their study of this stationary ribbed channel flow, Coletti *et al.* (2012, 2014) also conducted detailed PIV experiments to investigate the effects of spanwise system rotation on turbulent flow in a transverse rib-roughened rectangular duct. In their experiments, the measurement results of rotating duct flows were compared against those of a stationary smooth duct flow. The PIV experiments of Coletti *et al.* (2012, 2014) on rotating and non-rotating rib-roughened duct flows were later reproduced using a hybrid RANS–LES approach by Xun & Wang (2016), who used the PIV measurement data to validate a new forcing model applied to the RANS–LES interface.

1.3. *Research objectives*

Notwithstanding the previous contributions mentioned above, the number of detailed numerical studies on turbulent flow in a duct with transverse ribs is still limited, and many questions regarding the fundamentals of the flow physics remain open. Furthermore, no DNS results on rib-roughened duct flows have been published thus far. In view of this, we aim at performing a systematic DNS study of rib-roughened duct flows of three different blockage ratios ($Br = 0.05$, 0.1 and 0.2) to obtain detailed knowledge of the

rib height effects on the statistical moments and premultiplied energy spectra of the turbulent velocity field, local non-equilibrium of turbulence, large- and small-scale flow anisotropy, transport of turbulence kinetic energy (TKE), as well as the dynamics of mean and turbulent secondary flow motions. In order to identify the rib effects on the flow field, an additional DNS of a smooth duct flow has also been conducted at the same Reynolds number (as in the three rib cases), which is used as a baseline comparison case. This study also aims to bring new insights into the secondary flows and turbulence structures characteristic of a 3-D ribbed duct flow, which are considerably different from those of a conventional 2-D rough-wall boundary-layer flow.

The remainder of this paper is organized as follows. In § 2 the numerical algorithm for conducting DNS is introduced together with a detailed study of the minimum computational domain required for capturing dominant turbulent flow structures in a ribbed duct with various blockage ratios. Also in this section, in order to examine the predictive accuracy of the numerical approach, two additional simulations have been conducted based on two canonical test cases of (i) a 2-D ribbed plane-channel flow at $Re_b = 5600$, and (ii) a smooth duct flow at $Re_b = 4410$. Our DNS results of these two additional test cases are validated against those reported in the literature. In § 3 the influence of rib height on the statistically averaged quantities is analysed, including the mean flows, the pressure and viscous drag coefficients, Reynolds stresses, production and dissipation terms, budget balance of TKE, as well as the anisotropy of the turbulence field characteristic of the ribbed duct. Furthermore, the impact of rib height on sweep and ejection events is investigated. To this purpose, the third-order moments and the joint probability density functions (JPDF) of streamwise and vertical velocity fluctuations are studied. In § 4 the effect of rib height on the turbulent flow structures is analysed based on multiple tools such as vortex identifiers, two-point correlation functions and velocity spectra. Finally, in § 5 the major conclusions of this research are summarized.

2. Test cases and numerical method

Figure 1 shows a schematic of the computational domain for the ribbed squared duct with a side length D (i.e. $L_y = L_z = D$). The streamwise domain is $L_x = 6.4D$ long and consists of eight rib periods (P), with $P = 0.8D$. The height and width of the rectangular bars are H and W, respectively. In our analysis, it is useful to define the half side length ($\delta = D/2$), especially when the results are compared with those of a 2-D plane-channel flow. In our comparative study, DNS is performed based on three different blockage ratios (for $Br = H/L_y = 0.05$, 0.1 and 0.2). The flow field is assumed to be fully developed and periodic boundary conditions are applied to the inlet and outlet of the duct. A no-slip boundary condition is imposed on all solid walls. The Reynolds number is fixed at $Re_b = DU_b/\nu = 5600$, where U_b denotes the average bulk mean velocity over the streamwise direction of the ribbed duct. In comparison with a 2-D ribbed boundary-layer flow, more degrees of freedom are involved in the analysis of a 3-D ribbed duct flow. For instance, the restriction of spanwise homogeneity characteristic of a 2-D boundary-layer flow is lacking in a duct flow. Given the high blockage ratio, a common fixed-valued bulk Reynolds number Re_b is chosen, which facilitates a comparative study under a constant mass flow rate. This is similar to the study of Hirota *et al.* (1992) and Coletti *et al.* (2012), who conducted comparative experimental studies of rib-roughened duct flows based on bulk Reynolds number Re_b. The rib effects on the flow field are studied by comparing the DNS results of three rib cases against those of a baseline case of DNS of a smooth duct flow at the same Reynolds number Re_b. The geometrical set-up of the smooth duct

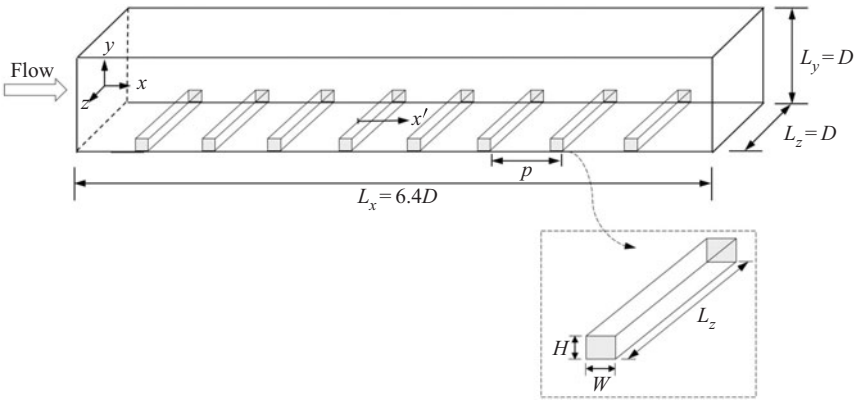

FIGURE 1. Schematic of a square duct with transverse ribs and coordinate system. The origin of the absolute coordinate system $[x, y, z]$ is located at the centre of the inlet y–z plane. Eight rib periods are simulated in the DNS. To facilitate the analysis of each rib period, the relative streamwise coordinate x' is defined, with its origin located at the windward face of each rib.

is similar to that described in figure 1, except that there are no ribs on the bottom wall and the streamwise length of the domain is $L_x = 6\pi\delta$ following the approach of Pirozzoli *et al.* (2018).

Table 1 compiles the flow parameters of three rib cases, including the Reynolds number based on the rib height (defined as $H^+ = Hu_{\tau R}/\nu$), streamwise domain length (defined as $L_x^+ = L_x u_{\tau R}/\nu$), elevation of the virtual origin (d_0) on the ribbed bottom wall side, and Reynolds numbers ($Re_{\tau S} = \delta u_{\tau S}/\nu$ and $Re_{\tau R} = \delta u_{\tau R}/\nu$) defined based on the mean streamwise wall friction velocities of smooth top and ribbed bottom walls (i.e. $u_{\tau S}$ and $u_{\tau R}$, respectively) in the central vertical (x–y) plane located at $z/\delta = 0$. The calculation of the value of $u_{\tau S}$ for the smooth top wall is straightforward, which is done based on the mean streamwise velocity gradient in the central x–y plane. The method for calculating the value of $u_{\tau R}$ for the ribbed bottom wall in the central x–y plane of the duct is analogous to that of Leonardi & Castro (2010) and Ismail, Zaki & Durbin (2018) for a 2-D ribbed turbulent channel flow, *viz.* $u_{\tau R}^2 = D_p + D_v$. Here, terms D_p and D_v are direct consequences of pressure and viscous drag forces in the central x–y plane, determined as

$$D_p = 1/(\rho L_x) \sum_{n=1}^{N} \int_0^H (\langle P_{wind} \rangle - \langle P_{lee} \rangle)\, \mathrm{d}y \quad \text{and} \quad D_v = \mu/(\rho L_x) \int_0^{L_x} (\partial \langle u \rangle / \partial y)_w\, \mathrm{d}x,$$

respectively. In these equations, the subscript 'w' denotes either the bottom wall or rib crest exposed to the streamwise flow, N is the total number of rib elements, $\langle\cdot\rangle$ denotes averaging over time and over the eight rib periods, and P_{wind} and P_{lee} represent the pressure on the windward and leeward faces of a rib, respectively. The position of the virtual origin in the central x–y plane can be determined analogously by following Thom (1971), Jackson (1981) and Chan *et al.* (2015), who studied 2-D rough-wall boundary-layer flows, *viz.*

$$d_0 = \int_0^H y D_t(y)\, \mathrm{d}y \Big/ \int_0^H D_t(y)\, \mathrm{d}y,$$

where $D_t = D_p + D_v$ is the total drag forcing term.

From table 1, it is clear that as the blockage ratio increases from $Br = 0.05$ to 0.2, the elevation of the virtual origin d_0/H increases monotonically as a result of an increasing

Br	D_p (m^2 s^{-2})	D_v (m^2 s^{-2})	H^+	L_x^+	d_0/H	$Re_{\tau R}$	$Re_{\tau S}$	Re_b
0.05	0.0095	0.00052	28	3587	0.38	280	183	5600
0.1	0.0167	−0.00143	69	4428	0.69	346	208	5600
0.2	0.0238	−0.00272	162	5203	0.84	406	236	5600

TABLE 1. Flow parameters for DNS of three ribbed square duct flow cases of different blockage ratios.

rib height; meanwhile, both values of $Re_{\tau S}$ and $Re_{\tau R}$ also increase monotonically. The increasing trend in the elevation of the virtual origin in the central x–y plane of a 3-D square duct observed here is similar to the DNS results of Bhaganagar *et al.* (2004) and Chan *et al.* (2015), who systematically investigated 2-D roughness boundary-layer flow in a plane channel and a circular pipe, respectively. The reason that the value of $Re_{\tau S}$ increases with the Br value is that this comparative study is conducted under the condition of a constant bulk Reynolds number Re_b. As the rib height increases, the mean streamwise velocity increases in order to maintain a constant mass flow rate. On the other hand, the physical mechanism underlying the monotonic increasing trend of $Re_{\tau R}$ with an increasing Br value is rather complicated. By definition, the value of $Re_{\tau R}$ is influenced by both values of D_p and D_v. From table 1, it is evident that the value of D_v is one order of magnitude smaller than that of D_p, indicating that the drag force is primarily contributed by the pressure drag term D_p, which increases as the rib height increases. It is interesting to observe that the value of the viscous drag term D_v transitions from being positive to being negative as the Br value increases. A negatively valued viscous drag is a direct reflection of boundary-layer separation in the recirculation bubble behind a rib. The rib height effects on the pattern of the recirculation bubble and on the spanwise variation of the viscous and pressure drag coefficients will be detailed shortly in § 3.1.

It should be indicated here that the calculation of the values of D_p, D_v, $Re_{\tau S}$, $Re_{\tau R}$ and d_0 in the central vertical (x–y) plane (located at $z/\delta = 0$) follows the method of analysis for a conventional 2-D rough-wall boundary layer. Strictly speaking, the value of applying this method to the analysis of a 3-D ribbed duct flow is very limited, simply because a 2-D boundary layer is absent in a 3-D ribbed duct flow and the analysis is restricted to the selected central vertical (x–y) plane. Furthermore, given the large value of the blockage ratio (up to $Br = 0.2$ in a square duct), it would be more reasonable to treat the tall ribs as part of the domain geometry rather than 2-D roughness elements.

Direct numerical simulation was performed with an in-house computer code developed using the FORTRAN 90/95 programming language and parallelized following the message passing interface (MPI) standard. In this computer code the continuity and momentum equations are discretized based on a general curvilinear coordinate system (ξ_1, ξ_2, ξ_3), and in the context of an incompressible flow, they are expressed as

$$\frac{1}{J}\frac{\partial\left(\beta_i^k u_i\right)}{\partial\xi_k} = 0, \tag{2.1}$$

$$\frac{\partial u_i}{\partial t} + \frac{1}{J}\frac{\partial}{\partial\xi_k}\left(\beta_j^k u_i u_j\right) = -\frac{1}{J\rho}\frac{\partial\left(\beta_i^k p\right)}{\partial\xi_k} - \frac{1}{\rho}\Pi\delta_{1i} + \frac{\nu}{J}\frac{\partial}{\partial\xi_p}\left(\frac{1}{J}\beta_j^p\beta_j^q\frac{\partial u_i}{\partial\xi_q}\right), \tag{2.2}$$

where u_i, p, ν, ρ and δ_{ij} represent the velocity, pressure, kinematic viscosity, density and Kronecker delta, respectively. In addition, Π denotes a constant streamwise pressure

gradient that drives the flow, and β_i^j and J denote the cofactor and Jacobian of tensor $\partial x_i/\partial \xi_j$, respectively. It is worth noting that this computational code is developed to tackle curved surfaces based on body-fitted mesh. Specific to the current application to simulation of the flow through a square duct with straight rectangular shaped ribs mounted on one wall, the Jacobian degenerates to Kronecker delta. The above governing equations are represented using tensor notations, and the streamwise (x), vertical (y) and spanwise (z) coordinates shown in figure 1 are denoted using x_i for $i = 1$, 2 and 3, respectively. Correspondingly, the three velocity components u, v and w are also denoted using u_1, u_2 and u_3. Eight rib periods are simulated in our DNS, and in our analysis of each rib period, we also use the relative streamwise coordinate x', with its origin located at the windward face of a rib (see figure 1).

This computer code has been successfully used for performing DNS of turbulent dispersion of passive concentration plumes in a channel flow (Noormohammadi & Wang 2019), and LES of turbulent flow and structures in a square duct roughened with perpendicular and V-shaped ribs (Fang *et al.* 2017). The numerical algorithm of the computer code is based on the finite-volume method in which a second-order accuracy is achieved with respect to both spatial and temporal discretizations. Within each sub-step of the second-order Runge–Kutta scheme, a fractional-step method is applied and a pressure correction equation is solved using the parallel algebraic multigrid solver, and the convergence of the solver is considered once the averaged residue of a discretized algebraic equation drops below 10^{-6}. For time advancement, the Courant–Friedrichs–Lewy number is approximately 0.2. A momentum interpolation approach is used to obtain the cell-face velocity components and based on the velocity and pressure values in two adjacent control volumes in order to avoid the potential checkerboard problem of the pressure field. The simulation started with an initial laminar flow solution superimposed with artificial perturbations to trigger turbulence. The precursor simulation was run for an extended duration of 73 flow-through times (i.e. $930\delta/U_b$) until the turbulent flow field becomes fully developed and statistically stationary. Then, turbulence statistics were collected for a time period over approximately 110 flow-through times (i.e. $1400\delta/U_b$). All the simulations were conducted using the WestGrid (Western Canada Research Grid) supercomputers. For each simulated case, 254 cores were used for performing DNS, and approximately 548 000 CPU hours were spent for solving the velocity field and for collecting the flow statistics (after the precursor simulation).

2.1. *Streamwise integral length scale and domain size*

In the current literature there are controversies over the proper choice of the streamwise computational domain size (L_x) for transient simulation of a ribbed turbulent duct flow. For instance, Sewall *et al.* (2006) performed LES to investigate the effects of transverse rib roughness on the turbulent flow and heat transfer within a square duct at a fixed Reynolds number. The streamwise domain in their LES was a single rib period (i.e. $L_x = P = 2\delta$) with a periodic boundary condition applied to the streamwise direction. Fang *et al.* (2017) studied turbulent flow and structures in a square duct with perpendicular and V-shaped ribs mounted on the bottom wall, and the streamwise domain size set to $L_x = 4.8\delta$. They showed that this domain size is insufficient for capturing the largest eddy structures in the duct centre. In view of this, a larger value of $L_x = 6.4D$ (or 12.8δ) is taken into account in the current DNS to ascertain that typical large-scale turbulent structures of the flow are properly captured. To confirm, streamwise two-point correlation (R_{uu}) is computed for different rib heights at various elevations. Note that since the flow in the vicinity

of ribs experiences various separation and reattachment phenomena, ribbed duct flow is remarkably inhomogeneous in the streamwise direction. Consequently, the two-point correlation of the fluctuating velocity components cannot be computed via fast Fourier transform. In this regard, we follow the approach of Christensen & Adrian (2001), who calculated auto- and cross-correlations of the velocity field in the physical space at several points across the vertical direction. For a ribbed duct flow, the streamwise two-point auto-correlation coefficient is defined as (Townsend 1980; Volino, Schultz & Flack 2009)

$$R_{uu}(x_{ref}, \Delta x) = \frac{\langle u'(x_{ref})u'(x_{ref} + \Delta x)\rangle}{\sqrt{\langle u'^2(x_{ref})\rangle \langle u'^2(x_{ref} + \Delta x)\rangle}}, \tag{2.3}$$

where u' represents the streamwise fluctuating velocity and Δx denotes the relative displacement from the reference point located at x_{ref}, such that $x = x_{ref} + \Delta x$.

Figure 2 compares the profiles of the normalized streamwise two-point auto-correlation coefficient at different elevations along the vertical line located at approximately the centre of the domain of $(x_{ref}/\delta, z_{ref}/\delta) = (5.9, 0.0)$ for two rib cases of different blockage ratios. In terms of the relative streamwise coordinate measured from the windward face of the upstream rib, the reference points are at $x'_{ref}/\delta = 0.4$. It is evident from this figure that R_{uu} decays to zero over one-half the streamwise domain length at all three elevations, indicating that the streamwise computational domain size is sufficiently large to capture energetic turbulence structures. By comparing figure 2(*a*) with 2(*b*), it is observed that as the rib height increases, the spread of the peak becomes greater as a result of larger streamwise length scales. Indeed, the streamwise integral length scale (i.e. $L_{xx} = \int_0^\infty R_{uu}(x)\,\mathrm{d}x$) of $Br = 0.2$ near the rib crest is 2.8 times that of $Br = 0.05$. From this figure, it is also clear that for the two rib cases of different Br values, the length scales of turbulent eddies slightly increase with an increasing distance from the rib crest in the vertical direction. Furthermore, from table 1, it is clear that as the blockage ratio increases from $Br = 0.05$ to 0.2, the non-dimensional domain length increases monotonically from $L_x^+ = 3587$ to 5203.

2.2. *Grid resolution*

In this study we used body-fitted mesh (BFM) to resolve precisely each rib geometry, such that the entire flow field can be accurately calculated. The simulations were conducted using $N_x \times N_y \times N_z = 1280 \times 148 \times 152$ body-fitted grid points. The mesh is non-uniform in all three directions, and is refined near all solid surfaces. It should be mentioned that there are two popular meshing methods in the current literature that can be used for dealing with riblets. Besides BFM, the immersed boundary method (IBM) can be also considered. The IBM method started with Peskin (1972) and has been significantly developed since (Mittal & Iaccarino 2005; Griffith & Patankar 2020). The IBM method has been successfully applied to DNS and LES of turbulent flows over regular and irregular shaped roughness elements (Leonardi *et al.* 2003; Orlandi *et al.* 2006; Scotti 2006; Bhaganagar 2008; Pinelli *et al.* 2010*a*; Lee, Sung & Krogstad 2011; Yuan & Piomelli 2014; Bhaganagar & Chau 2015; Rouhi, Chung & Hutchins 2019). As two popular methods, both BFM and IBM have advantages and disadvantages. In comparison with the BFM method, the IBM method is computationally less expensive, but it relies on an additional roughness-forcing model. Given that the blockage ratio is relatively high (up to $Br = 0.2$), the tall ribs should be treated as part of the domain geometry rather than 2-D roughness elements. Furthermore, because the geometry of the square rib bars is regular and simple, we can use BFM to resolve precisely each rib geometry (without a need for

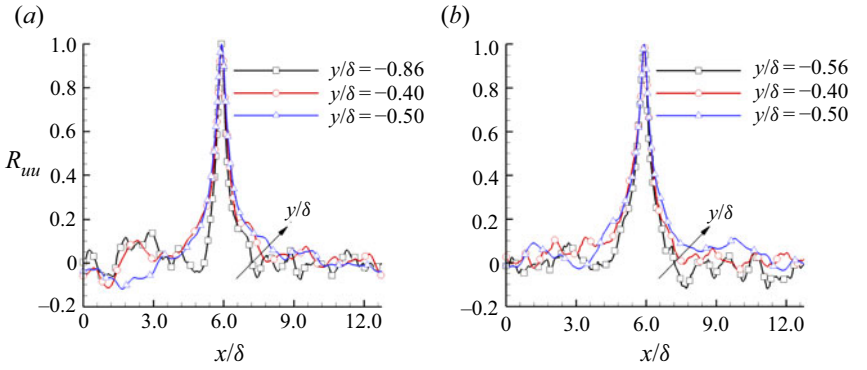

FIGURE 2. Streamwise profiles of two-point auto-correlations for ribbed duct flows of two different blockage ratios (Br) at different elevations (y/δ). The reference points are located approximately at the centre of the computational domain (i.e. at $x_{ref}/\delta = 5.9$ and $z_{ref}/\delta = 0.0$). In terms of the relative streamwise coordinate measured from the windward face of the upstream rib, the reference points are at $x'_{ref}/\delta = 0.4$. In the vertical direction, the reference points at $y/\delta = -0.86$ and -0.56 coincide with the peaks positions of $\langle u'u' \rangle$ and $-\langle u'v' \rangle$ for $Br = 0.05$ and 0.2 cases, respectively (which will be demonstrated later in § 3.3). (*a*) $Br = 0.05$ and (*b*) $Br = 0.2$.

a roughness-forcing model as in IBM), such that the flow field of the entire computation domain (including the rib neighbourhood) can be accurately calculated. The BFM method used here is similar to those of Ikeda & Durbin (2007), Yang & Shen (2010), Philips, Rossi & Iaccarino (2013), Chan *et al.* (2015), Wagner & Shishkina (2015), MacDonald *et al.* (2016), and Ismail *et al.* (2018), who directly resolved regularly shaped roughness elements (e.g. ribs, cubes and wavy surfaces) using body-fitted meshes.

To ensure that this mesh is sufficiently fine to capture the smallest scales of the turbulence as demanded by DNS, the ratio of the grid size to the Kolmogorov length scale is investigated. Based on their DNS study of turbulent channel flows, Moser & Moin (1987) indicated that the grid size requires to be of the same order as the Kolmogorov length scale (i.e. $O(\Delta/\eta) \sim O(1)$) in order to accurately capture the turbulence kinetic energy dissipation pertaining to the smallest scales of turbulence. The grid size considered here is based on the maximal dimension of a grid cell in all three directions (i.e. $\Delta = \max(\Delta_x, \Delta_y, \Delta_z)$) and the Kolmogorov length scale is calculated as $\eta = (\nu^3/\varepsilon)^{1/4}$, where the local dissipation rate is defined as $\varepsilon = \nu\langle \partial u'_i/\partial x_j \partial u'_i/\partial x_j \rangle$.

The contours of Δ/η in the central x–y plane for two different rib cases are shown in figure 3. As indicated in figures 3(*a*) and 3(*b*), it is apparent that the value of Δ/η is of the order of one (i.e. $\Delta/\eta = O(1)$) in the two rib cases. Furthermore, as is seen in figures 3(*a*) and 3(*b*), the maximum value of Δ/η is found to be around 6.2 at the leading corner of the rib. Other than this specific location, the value of Δ/η never exceeds 4.5 over the rest of the computational domain for all the simulations. This indicates that this grid spacing suffices for accurately performing DNS of turbulent flows in all three ribbed duct cases tested. Contours of a non-dimensionalized grid size shown in figure 3 are comparable to those used by Ikeda & Durbin (2007), who conducted a DNS study of the 2-D turbulent boundary layer over periodic transverse rib roughness, and are finer than those employed for DNS of a turbulent flow over cuboidal obstacles mounted on a wall conducted by Coceal *et al.* (2007). The spatial resolutions used in our DNS are summarized in table 2.

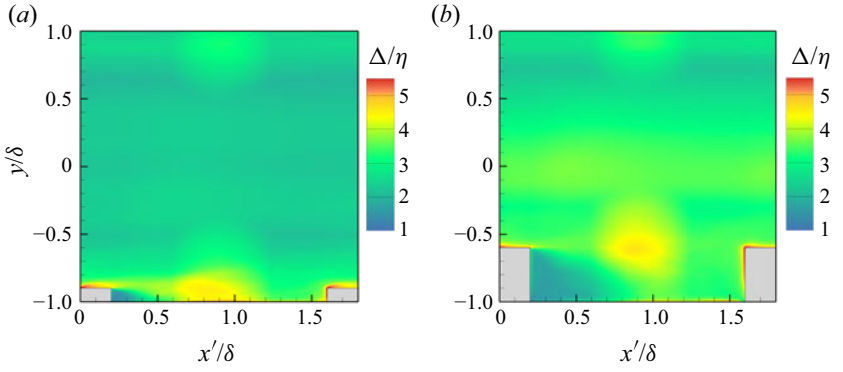

FIGURE 3. Contours of the ratio of the grid size to the Kolmogorov length scale (Δ/η) in the central plane at $z/\delta = 0.0$ for two different blockage ratios of (*a*) $Br = 0.05$ and (*b*) $Br = 0.2$.

Br	$\Delta_x^+\|_{max}$	$\Delta_y^+\|_{max}$	$\Delta_z^+\|_{max}$	$\Delta_x^+\|_{min}$	$\Delta_y^+\|_{min}$	$\Delta_z^+\|_{min}$
0.05	6.5	5.4	5.9	0.65	0.48	0.61
0.1	7.7	6.5	7.2	0.69	0.57	0.69
0.2	8.9	7.9	8.1	0.73	0.68	0.76

TABLE 2. Grid resolutions in wall units for all three directions based on the mean streamwise wall friction velocity ($u_{\tau S}$) along the intersection line of the smooth top wall (located at $y = \delta$) and the central vertical (x–y) plane (located at $z/\delta = 0$).

2.3. *Code validation*

Prior to our DNS study of ribbed square duct flows, the computer code was validated based on two classical test cases of (1) a smooth square duct flow at $Re_b = 4410$, and (2) a 2-D ribbed plane-channel flow (with spanwise square bars mounted on one wall) at $Re_b = 5600$. Our DNS results were compared against the reported DNS data of Gavrilakis (1992), Pinelli *et al.* (2010*b*), Vinuesa *et al.* (2014), and Pirozzoli *et al.* (2018) on the smooth duct flow case, and with those of Orlandi *et al.* (2006) and Ismail *et al.* (2018) on the 2-D ribbed planed-channel flow case. The comparisons are shown in figures 4 and 5, respectively.

The DNS of the smooth duct flow was performed with a computational domain of $L_x \times L_y \times L_z = 6\pi\delta \times 2\delta \times 2\delta$. The streamwise computational domain was set to $L_x = 6\pi$, identical to that used in Pirozzoli *et al.* (2018). A periodic boundary condition was applied to the streamwise direction and a no-slip boundary condition was prescribed at all four sidewalls. The number of grid points used in our DNS was $N_x \times N_y \times N_z = 512 \times 128 \times 128$, identical to that used for 'case A' of the DNS study by Pirozzoli *et al.* (2018). As is evident in figure 4, our DNS results show an excellent agreement with the reported data in terms of the prediction of the non-dimensionalized mean transverse velocity $\langle v \rangle / U_b$ and root-mean-squares (RMS) of the streamwise velocity fluctuations u_{rms}/U_b. Figure 4(*a*) clearly indicates the presence of the secondary mean flow in the cross-stream directions, as the magnitude of $\langle v \rangle / U_b$ is non-negligible, and the profile is characterized by a 'S-shaped' pattern along the vertical direction. From figure 4(*b*), it is seen that the profile of non-dimensionalized streamwise RMS velocity u_{rms}/U_b manifests

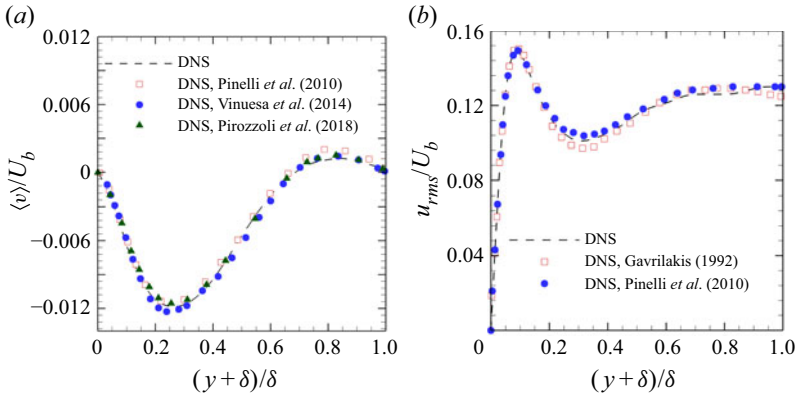

FIGURE 4. Comparison of the vertical profiles of mean transverse velocity $\langle v\rangle$ and streamwise RMS velocity u_{rms} against the reported DNS data of Gavrilakis (1992), Pinelli *et al.* (2010*b*), Vinuesa *et al.* (2014) and Pirozzoli *et al.* (2018) for a smooth square duct flow of $Re_b = 4410$ in the off-centre vertical planes located at $z/\delta = -0.75$ and -0.7, respectively. (*a*) Profiles of $\langle v\rangle$ at $z/\delta = -0.75$ and (*b*) profiles of u_{rms} at $z/\delta = -0.7$.

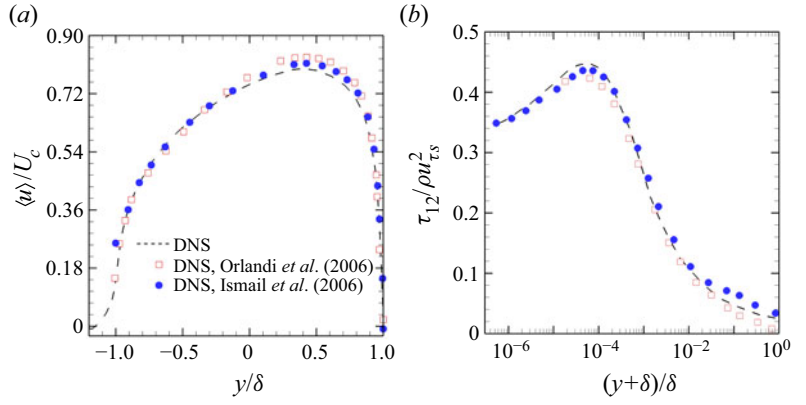

FIGURE 5. Comparison of the vertical profiles of mean streamwise velocity $\langle u\rangle$ and viscous shear stress τ_{12} against the DNS data of Orlandi *et al.* (2006) and Ismail *et al.* (2018) for 2-D turbulent plane-channel flow of $Re_b = 5600$ with transverse square ribs mounted on one wall. (*a*) Profiles of $\langle u\rangle$ and (*b*) profiles of τ_{12}.

a primary peak near the sidewall, and again increases in value close to the duct centre. Clearly, in a smooth duct flow, the presence of the secondary flow has a significant impact on the mean and turbulence fields. Later, we will show that the occurrence of the secondary flow is characteristic of both smooth and ribbed duct flows, which is due to the confinement of the four sidewalls of the duct.

For the second test case of a 2-D ribbed plane-channel flow, the DNS was performed in a computational domain of $L_x \times L_y \times L_z = 8\delta \times 2.2\delta \times \pi\delta$ consisting of five rib periods, identical to the set-up of Orlandi *et al.* (2006). The same test case has also been investigated by Ismail *et al.* (2018), and their data are also used here in our comparative study. A periodic boundary condition was applied to both streamwise and spanwise directions, and a no-slip boundary condition was applied to all surfaces. Following Orlandi *et al.* (2006), the range of the vertical coordinate is $-1.2 \leq y/\delta \leq 1.0$. The number of grid

points used in our DNS was $N_x \times N_y \times N_z = 400 \times 160 \times 128$, identical to that used by Orlandi *et al.* (2006). Figure 5 compares the predicted mean streamwise velocity and mean viscous shear stress profiles against the DNS data of Orlandi *et al.* (2006) and Ismail *et al.* (2018). As shown in figure 5, our results are in an excellent agreement with the reported data. The effects of ribs on the velocity field is evident in both figures 5(*a*) and 5(*b*). The vertical profile of $\langle u \rangle / U_c$ becomes asymmetrical in the vertical direction due to the presence of the ribs. Here, $U_c = 3U_b/2$ is the mean streamwise velocity at the centre line of the channel (Orlandi *et al.* 2006; Ismail *et al.* 2018). From figure 5(*a*), it is also clear that the shear layer carrying the highest streamwise momentum is pushed towards the smooth top wall. These characteristics of the mean streamwise velocity profile further result in a viscous shear stress ($\tau_{12} = \mu \partial \langle u \rangle / \partial y$) profile that is special for a 2-D ribbed boundary-layer flow shown in figure 5(*b*). The viscous shear stress reaches its maximum near the rib crest and decreases as the channel centre is approached.

3. Statistics of the velocity field

3.1. *Mean velocity field and mean flow structures*

Figure 6 compares the time-averaged streamlines in the central plane located at $z/\delta = 0.0$ for three different rib blockage ratios. This figure clearly shows the effect of rib height on the mean flow structures. As is seen in figure 6(*a–c*), the mean flow structures between the ribs consist of a large recirculation bubble (marked with 'B'), and two small secondary vortices located at corners on the leeward side of the upstream rib and windward side of the downstream rib (marked with 'A' and 'E', respectively). By comparing these figures, it is clear that corner vortex A is not apparently observed at $Br = 0.05$ due to the fact that the rib is not high enough to cause a significant sudden expansion of the flow in the lee of the rib. The size of corner vortex A increases as the rib height increases. Owing to the relatively small velocity (roughly 15 % of the free-stream velocity) within the recirculation zone B, an adverse pressure gradient is induced, causing the flow to reattach onto the bottom wall. Downstream of the reattachment point 'C', a new boundary layer builds up and impinges on the next rib leading to the generation of the upstream vortex 'E' (starting at point 'D'). Clearly, the recirculation bubble B becomes increasingly elongated with an increasing rib height, which further leads to a reduction in the horizontal distance between points C and D. This phenomenon inevitably impacts both the local friction and form drags (which will be discussed in § 3.2). By comparing figure 6(*a–c*), it is interesting to observe that the mean flow patterns of cases $Br = 0.05$ and 0.1 are typical of k-type rough-wall flows, but that of $Br = 0.2$ exhibits features that are characteristic of a d-type rough-wall flow. Specifically, as shown in figure 6(*c*), recirculation bubble B is well extended such that it occupies almost the entire 'cavity' between two adjacent ribs, there is no touch point D, and the mean free-stream flow skims over the cavity. The pitch-to-height ratios of these three rib cases are $P/H = 16$, 8 and 4 (for $Br = 0.05$, 0.1 and 0.2), respectively. If we strictly follow the proposal of Perry *et al.* (1969) and Bandyopadhyay (1987) on 2-D rough-wall boundary layers, all these three rib cases should be considered as k-type rough-wall flows because their pitch-to-height ratios are larger than three. However, the 3-D rough-wall flow in a square duct under current investigation is qualitatively different from the classical case of 2-D rough-wall boundary-layer flow. As such, the case of $Br = 0.2$ features a d-type rough-wall flow pattern.

To assess the effects of the rib height on the velocity field, the non-dimensional vertical profiles of the mean streamwise velocity at different relative streamwise locations ($x'/\delta = 0.4$, 1.0 and 1.5) are plotted in figure 7. The results of three rib cases are compared

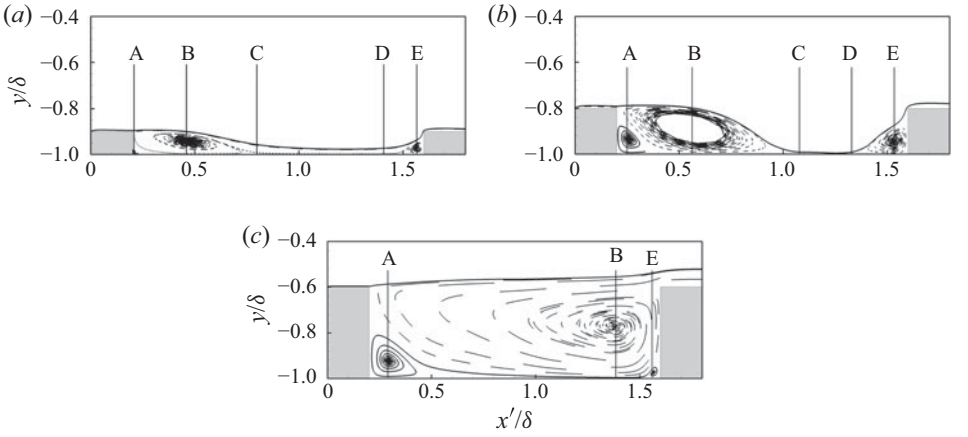

FIGURE 6. Mean streamline pattern near the ribbed bottom wall in the central plane located at $z/\delta = 0.0$ for three different rib cases of $Re_b = 5600$. (*a*) $Br = 0.05$, (*b*) $Br = 0.1$ and (*c*) $Br = 0.2$.

with that of the smooth duct in the central vertical plane (located at $z/\delta = 0$). As expected, the profile of $\langle u \rangle / U_b$ of the smooth duct flow is symmetrical in the vertical direction. By contrast, the profiles of all three rib case are 'skewed' towards the smooth top wall. By comparing figure 7(*a–c*), it is seen that the vertical position corresponding to the maximum value of the mean streamwise velocity elevates from $y/\delta = -0.07$ to 0.28 as the blockage ratio increases from $Br = 0.05$ to 0.2. Owing to the presence of the ribs, the magnitude of the mean streamwise velocity $\langle u \rangle / U_b$ is smaller than that of the smooth duct flow on the ribbed bottom wall side. As the rib height increases, the profile of the mean streamwise velocity shifts downwards progressively, a pattern that is often seen in a 2-D rough-wall boundary-layer with spanwise homogeneity. By contrast, on the smooth top wall side, the magnitude of the mean streamwise velocity increases monotonically as the rib height increases. This is due to the need of maintaining a constant mass flow rate under the test condition of a constant bulk Reynolds number Re_b. Clearly, as the rib height increases, the flow convects downstream with higher momentum near the duct centre associated with a decrease in the mean streamwise velocity in the near-wall region below the rib height. Furthermore, owing to the presence of the ribs, the mean streamwise velocity is bumped up around the rib crest. From figure 7(*a–c*), it is apparent that the shear layer strength, as interpreted from the vertical gradient of the mean streamwise velocity, decreases monotonically in the region immediately above the rib crest as the rib height increases (i.e. the value of $|\mathrm{d}\langle u \rangle / \mathrm{d}y|$ at the rib crest decreases as the blockage ratio increases from $Br = 0.05$ to 0.2). These mean flow features directly influence the large-scale eddies induced by the roll-up of the shear layer near the rib crest, which have a significant impact on the turbulent transport processes.

The study of the mean streamwise velocity can be refined by further examining the effects of rib height on the mean viscous shear stress $\tau_{12} = \mu \partial \langle u \rangle / \partial y$ in the central vertical plane (located at $z/\delta = 0$), which is shown in figure 8. From figure 8(*a–c*), it is clear that the profile of τ_{12} is symmetrical for the smooth duct flow, but asymmetrical for all three ribbed duct cases at all three relative streamwise locations of $x'/\delta = 0.4$, 1.0 and 1.5. As indicated by the dominant peak of τ_{12} shown in figure 8(*a–c*), it is clear that the shearing effect is the highest near the rib crest (in the vertical direction) and at $x'/\delta = 0.4$ relative to the windward face of the upstream rib (in the streamwise direction) in all three

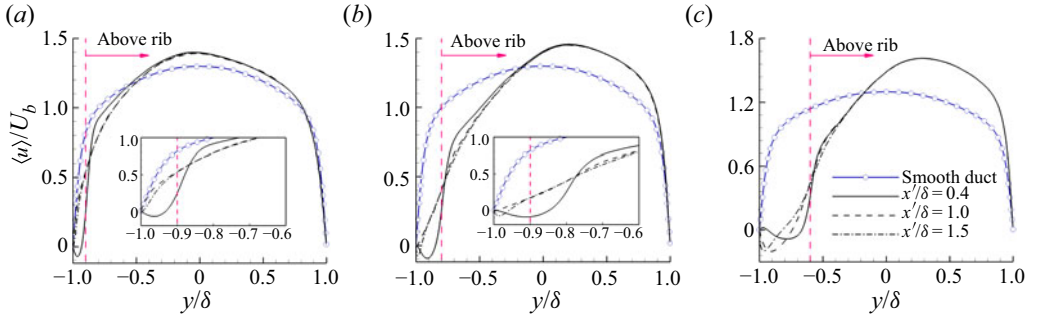

FIGURE 7. Comparison of the non-dimensionalized mean streamwise velocity profiles at three relative streamwise locations (for $x'/\delta = 0.4$, 1.0 and 1.5) in the central plane (located at $z/\delta = 0$) of the ribbed square duct flows (of three blockage ratios for $Br = 0.05$, 0.1 and 0.2) with that of the smooth square duct flow at the same Reynolds number $Re_b = 5600$. The vertical pink dashed line demarcates the rib crest. (*a*) $Br = 0.05$, (*b*) $Br = 0.1$ and (*c*) $Br = 0.2$.

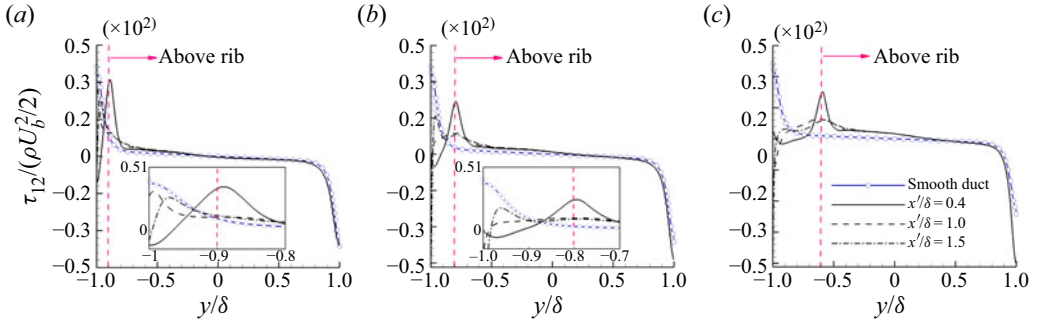

FIGURE 8. Comparison of the non-dimensionalized mean viscous shear stress profiles at three relative streamwise locations (for $x'/\delta = 0.4$, 1.0 and 1.5) in the central plane (located at $z/\delta = 0$) of the ribbed square duct flows (of three blockage ratios for $Br = 0.05$, 0.1 and 0.2) with that of the smooth square duct flow at the same Reynolds number $Re_b = 5600$. The vertical pink dashed line demarcates the rib crest. (*a*) $Br = 0.05$, (*b*) $Br = 0.1$ and (*c*) $Br = 0.2$.

rib cases. This feature is in sharp contrast to that of the smooth duct flow, in which the value of τ_{12} is the maximum at the two walls. From figures 7 and 8, it is understood that magnitudes of both the mean streamwise velocity gradient $|\mathrm{d}\langle u\rangle/\mathrm{d}y|$ and viscous shear stress τ_{12} are the largest near the rib crest at $x'/\delta = 0.4$ in all three rib cases. A large value of the mean streamwise velocity gradient often leads to high turbulent production rate and TKE level. In view of this, in the remainder of our analysis, we pay close attention to this special relative streamwise location $x'/\delta = 0.4$. Also, it is noticed that this particular relative streamwise position was also used by Coletti *et al.* (2012) in their PIV experimental study of turbulent flow and structures in a ribbed duct with and without system rotations.

To understand the influence of secondary motions on the mean streamwise velocity field, figure 9 demonstrates the contours of the non-dimensionalized mean streamwise vorticity (defined as $\langle\omega_x\rangle = \partial\langle w\rangle/\partial y - \partial\langle v\rangle/\partial z$) and the magnitude of the non-dimensionalized mean streamwise velocity $\langle u\rangle/U_b$ (superimposed with the mean spanwise-vertical velocity vectors) in the cross-stream (y–z) plane located at $x'/\delta = 0.4$. Given the central symmetry of the flow field, only one half of the cross-stream domain is shown. As is evident from the mean velocity vector map shown in figure 9, in all three rib cases, there exists one

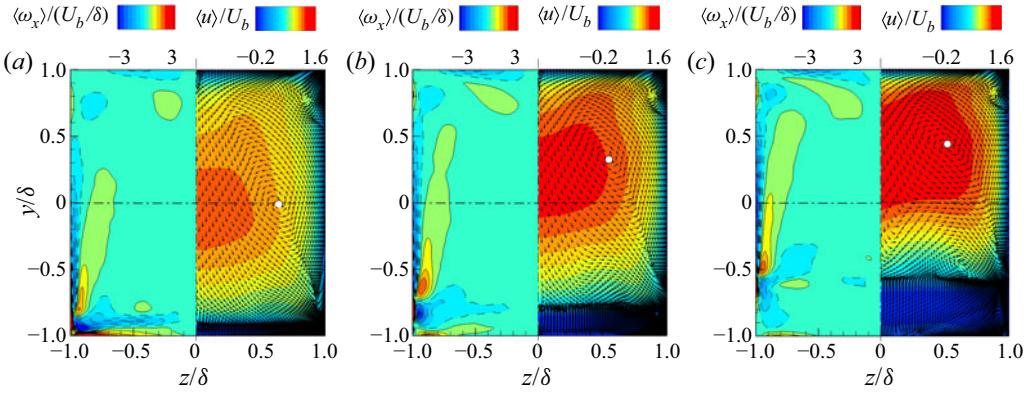

FIGURE 9. Contours of non-dimensionalized mean streamwise vorticity $\langle\omega_x\rangle/(U_b/\delta)$ (left), and the magnitude of the non-dimensionalized mean streamwise velocity $\langle u\rangle/U_b$ superimposed with the mean spanwise-vertical velocity vectors (right) in the y–z plane at the relative streamwise location $x'/\delta = 0.4$ for different blockage ratios. White dots denote the centre of the secondary flow vortex. The vectors are displayed at every four spanwise grid points and every three vertical points to ensure a clear view of the velocity field. (a) $Br = 0.05$, (b) $Br = 0.1$ and (c) $Br = 0.2$.

large streamwise-elongated vortex on each side of the duct. The appearance of this pair of large vortices is a reflection of the mean secondary flows in the cross-stream plane. The centres of these two vortices can be located using the vector map and are marked using white dots in figure 9. The mean secondary flows exhibit two apparent trends as the rib height increases. Firstly, the vortex centre shifts upwards and transversely to the sidewalls as the rib height increases. Specifically, the centre of the vortex lies at $(y/\delta, z/\delta) = (-0.01, 0.64)$ for $Br = 0.05$, but moves to (0.32, 0.55) and (0.42, 0.51) as the blockage ratio increases to $Br = 0.1$ and 0.2, respectively. Secondly, the impingement region on the sidewalls occurs at a higher elevation as the rib height increases. The secondary flow patterns demonstrated using the non-dimensionalized mean streamwise vorticity $\langle\omega_x\rangle/(U_b/\delta)$ in figure 9(a–c) are consistent with those shown using the mean spanwise-vertical velocity vectors. However, the criterion based on $\langle\omega_x\rangle/(U_b/\delta)$ is advantageous in differentiating vortices of opposite rotating directions. Figure 9(a–c) also shows that the magnitude of $\langle\omega_x\rangle/(U_b/\delta)$ decreases near the bottom corner of the ducts as the blockage ratio increases; however, the magnitude of $\langle\omega_x\rangle/(U_b/\delta)$ in regions adjacent to the side and top walls increases monotonically with an increasing rib height. For example, in the region close to the vertical sidewall (for $-1.0 < z/\delta < -0.95$) the strength of $\langle\omega_x\rangle/(U_b/\delta)$ for the case of $Br = 0.2$ is approximately 1.7 and 1.4 times larger than those of $Br = 0.05$ and 0.1, respectively.

3.2. *Viscous and pressure drags*

To better understand the effects of rib height on the mean flow, the distributions of the skin friction and pressure coefficients are demonstrated in the x–z plane (located below the rib height) in figures 10 and 11, respectively. The skin friction and pressure coefficients are defined as $C_f = \tau_w/(\rho U_b^2/2)$ and $C_p = \langle p\rangle/(\rho U_b^2/2)$, respectively, where τ_w represents the local total wall friction stress calculated as $\tau_w = \mu\left[(\partial\langle u\rangle/\partial y)^2 + (\partial\langle w\rangle/\partial y)^2\right]_w^{1/2}$. Figure 10 clearly shows that the formed mean flow structures affect considerably the spatial

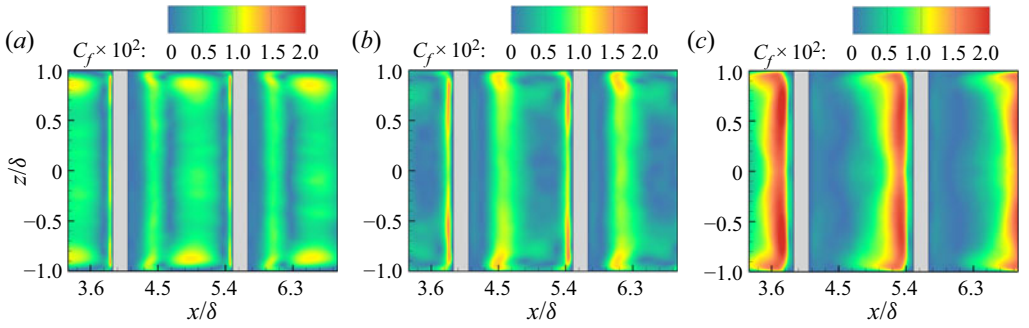

FIGURE 10. Contours of the skin friction coefficient C_f in the x–z plane on the bottom wall located at $y/\delta = -1.0$ for three different rib cases. (a) $Br = 0.05$, (b) $Br = 0.1$ and (c) $Br = 0.2$.

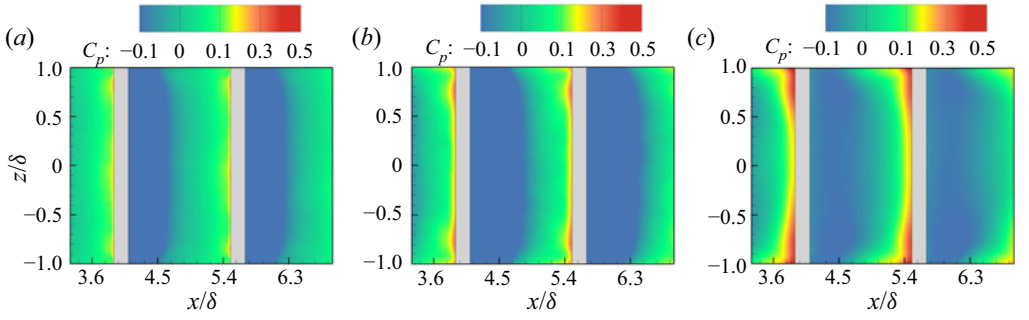

FIGURE 11. Contours of the pressure coefficient C_p in the x–z plane at half rib height for three different rib cases. (a) $Br = 0.05$ at $y/\delta = -0.95$, (b) $Br = 0.1$ at $y/\delta = -0.9$ and (c) $Br = 0.2$ at $y/\delta = -0.8$.

distribution of the skin friction coefficient. From this figure, it is clear that the highest value of C_f occurs around the leeward and windward faces of the ribs corresponding to the cores of the recirculation bubble B and upstream vortex E, respectively (see figure 6). As also shown in this figure, the effects of sidewalls on the corner vortex A and recirculation bubble B are found to be negligible in the central region (for $-0.5 < z/\delta < 0.5$), leading to a uniform spanwise distribution of C_f in this region. However, as the sidewall is approached, the value of C_f enhances significantly to reflect the boundary-layer effect near the two sidewalls of the duct (see figure 9). This result is consistent with the findings of Casarsa & Arts (2005) who conducted a PIV experimental study of turbulent flow in a square duct with square rib bars (of a high blockage ratio of $Br = 0.3$) mounted on one wall in a wind tunnel.

In figure 11 the spatial distribution of the pressure coefficient C_p for the three ribbed duct cases is plotted in the x–z plane located at the middle height of the rib. As is clear in this figure, the pressure drag is mostly contributed by the pressure difference between the windward and leeward faces of the rib. From figure 11(a–c), it is observed that the magnitude of C_p near the windward face of the rib increases with an increasing rib height, indicating an enhanced impinging effect of the flow. The variation of the mean pressure value with the blockage ratio shown in figure 11 is consistent with the vortex pattern of the mean flow exhibited in figure 6. As the blockage ratio increases from $Br = 0.05$ to 0.1, the size of vortex E increases, which results in a stronger impinging effect on the windward rib face. However, as the Br value further increases from 0.1 to 0.2, the

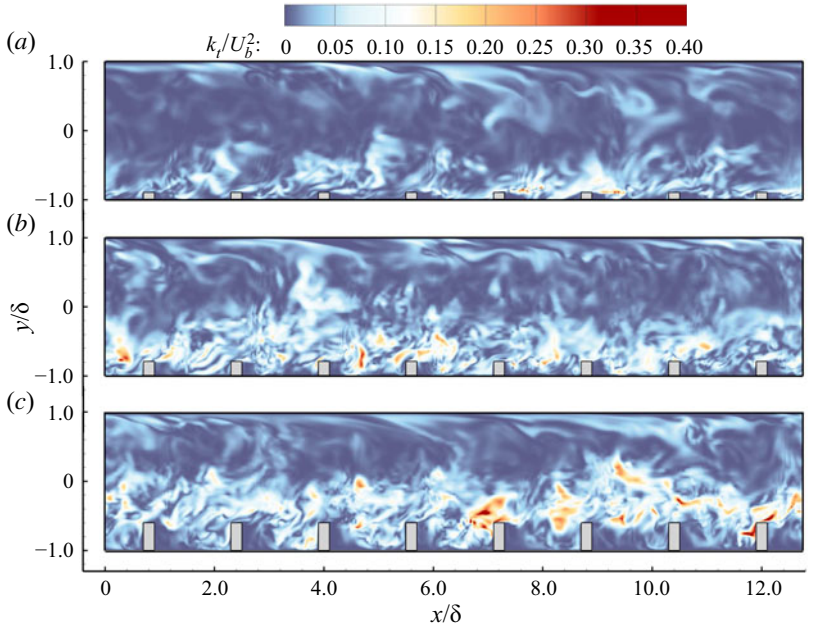

FIGURE 12. Contours of the instantaneous turbulent kinetic energy $k_t = (u'^2 + v'^2 + w'^2)/2$ (non-dimensionalized using U_b^2) in the central x–y plane located at $z/\delta = 0.0$ for three different rib cases. (*a*) $Br = 0.05$, (*b*) $Br = 0.1$ and (*c*) $Br = 0.2$.

mechanism underlying the vortex impinging effect changes fundamentally. By comparing figure 6(*c*) with 6(*b*), it is clear that the size of vortex B (instead of vortex E) increases significantly as the blockage ratio increases from $Br = 0.1$ to 0.2 and, consequently, the impinging effect of the flow on the windward face of the rib is dominated by vortex B instead of vortex E.

3.3. *Turbulent stresses*

Figure 12 compares the contours of 'instantaneous turbulent kinetic energy' (defined as $k_t = \left(u'^2 + v'^2 + w'^2\right)/2$, following the approach of Ikeda & Durbin 2007; Ismail *et al.* 2018) in the central x–y plane of different rib cases. From the qualitative results shown in the figure, it is intuitive that the characteristic length scales of turbulence are sensitive to the rib height. From figure 12, it is evident that owing to the disturbances from the ribs, the magnitude of k_t in all three rib cases is greatly enhanced on the ribbed bottom wall side than on the smooth top wall side. Near the rib crest, unsteady eddies are triggered, which shed into the flow above the rib crest and then are convected downstream. From figure 12, it is clear that although the TKE production rate is the highest at the rib crest, the k_t value is actually low in the vicinity of the rib crest (due to the no-slip boundary condition). Owing to the strong streamwise convection, the instantaneous TKE level is typically higher downstream of the rib crest. Clearly, as the blockage ratio increases from $Br = 0.05$ to 0.2, the intensity of the spanwise vortices generated near the rib crest increases, resulting in an enhancement of local turbulent transport of momentum and energy between the ribbed bottom wall and duct centre.

Figure 13 compares the vertical profiles of Reynolds stresses of three rib cases along the central vertical line located at $(x'/\delta, z/\delta) = (0.4, 0.0)$. The results of the three rib cases are compared against that of the smooth duct in the central vertical plane located at $z/\delta = 0$.

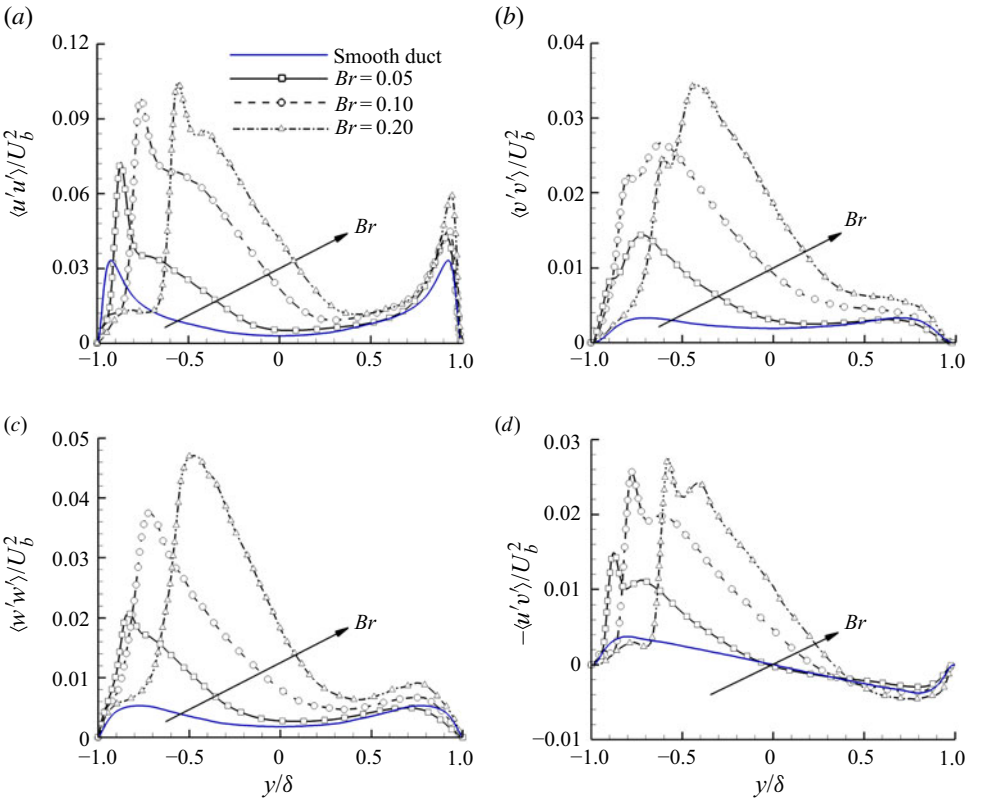

FIGURE 13. Vertical profiles of Reynolds normal ($\langle u'u'\rangle$, $\langle v'v'\rangle$ and $\langle w'w'\rangle$) and shear ($-\langle u'v'\rangle$) stresses along the vertical line positioned at $(x'/\delta, z/\delta) = (0.4, 0.0)$ for three ribbed square duct flows of different blockage ratios (of $Br = 0.05$, 0.1 and 0.2), in comparison with those of the smooth duct flow. (*a*) Profiles of $\langle u'u'\rangle$, (*b*) profiles of $\langle v'v'\rangle$, (*c*) profiles of $\langle w'w'\rangle$ and (*d*) profiles of $-\langle u'v'\rangle$.

Characteristic of a smooth duct flow, the profiles of the Reynolds normal and shear stresses are symmetrical and anti-symmetrical about the duct centre ($y/\delta = 0$), respectively. By contrast, the profiles of all Reynolds stress components are asymmetrical in all three rib cases due to the presence of the ribs. As is evident in figure 13, in general, the magnitudes of the Reynolds normal and shear stresses of the ribbed duct flows are much larger than those of the smooth duct flow due to the disturbances from the ribs. Furthermore, it is apparent the turbulence level as indicated by the magnitudes of the Reynolds normal and shear stresses are much larger on the ribbed bottom wall side than on the smooth top wall side. From figure 13(*d*), it is clear that the value of Reynolds shear stress $-\langle u'v'\rangle/U_b^2$ of the three ribbed cases is comparable to that of the smooth square duct flow in the central vertical plane. However, the magnitude of $-\langle u'v'\rangle/U_b^2$ is much smaller near the smooth top wall than near the ribbed bottom wall. This observation is consistent with the findings of Wang *et al.* (2007), Coletti *et al.* (2012) and Fang *et al.* (2015), who conducted PIV experiments of ribbed duct flows of a similar set-up, and with the LES results of ribbed square duct flows of Xun & Wang (2016) and Fang *et al.* (2017).

For all three rib cases, the highest Reynolds stress levels occur slightly above the rib crest, where the shear effect (as indicated by the magnitude of the vertical mean velocity gradient $\partial\langle u\rangle/\partial y$, see figure 7) is the greatest. Specifically, for the $\langle u'u'\rangle$, $\langle w'w'\rangle$ and

$-\langle u'v'\rangle$ components, their peak values on the ribbed wall side occur around $y/\delta = -0.86$, -0.76 and -0.56 for $Br = 0.05$, 0.1 and 0.2, respectively. As clearly shown in this figure, the peak values of the Reynolds normal ($\langle u'u'\rangle$, $\langle v'v'\rangle$ and $\langle w'w'\rangle$) and shear ($-\langle u'v'\rangle$) stress components are progressively enhanced near the rib crest with an increasing rib height, a feature that is fully consistent with the qualitative result shown in figure 12. This enhancement is mainly owing to the promotion of the shear layer strength emanating from the rib crest, which further augments the TKE production term, $-\langle u_i'u_j'\rangle \partial\langle u_i\rangle/\partial x_j$. This observation is also consistent with the DNS result of Nagano, Hattori & Houra (2004), who studied the effects of rib height on the turbulence statistics in a 2-D plane-channel flow. They reported that the high level of turbulence energy is attributed to large values of blockage ratios. From figure 13(*a–c*), it is evident that the magnitudes of normal components decrease as the duct centre is approached. Furthermore, it is interesting to observe that the discrepancies between the streamwise, vertical and spanwise Reynolds normal stresses near the rib crest decrease monotonically as the blockage ratio increases from $Br = 0.05$ to 0.2, leading to an enhanced degree of isotropy. As is evident in figure 13(*d*), similar to the normal components, the magnitude of the Reynolds shear stress component $-\langle u'v'\rangle$ also becomes insignificant upon approaching the duct centre. Because the value of $-\langle u'v'\rangle$ is contributed by the ejection and sweep events, this indicates that the strength of these events decreases significantly in the central region, especially for $0.0 < y/\delta < 0.5$. As the smooth top wall is approached, the Reynolds normal and shear stress profiles displayed in figure 13 become increasingly similar to those of the classical turbulent channel flow (Kim, Moin & Moser 1987). Later in §§ 3.6 and 3.7, we will refine our discussion by examining the blockage effects on the Reynolds stress anisotropy tensor and by conducting a quadrant analysis of the ejection and sweep events.

To demonstrate the 3-D effects of the ribbed duct flow, figure 14 compares the spanwise profiles of the Reynolds normal ($\langle u'u'\rangle$, $\langle v'v'\rangle$ and $\langle w'w'\rangle$) and shear ($-\langle u'v'\rangle$) stresses along elevated lines positioned at $(x'/\delta, y/\delta) = (0.4, -0.6)$, $(0.4, -0.5)$ and $(0.4, -0.3)$ for three blockage ratios of $Br = 0.05, 0.1$ and 0.2, respectively. Given the different heights of ribs in the three test cases, these three positions are all at the same relative elevation that is 0.3δ (or, $0.15D$) above the rib crest in each case. As shown in figure 14, the maximum intensity of $\langle u'u'\rangle$ occurs in a region between the sidewall and centre of the duct (e.g. for the $Br = 0.2$ case, the profile peaks at $z/\delta \approx \pm 0.4$). Furthermore, it is seen that the peak position of $\langle u'u'\rangle$ shifts towards the duct centre as the rib height increases, a pattern that is consistent with the qualitative results shown in figure 12. As is clearly seen from figure 14(*a–c*), for the three rib cases tested, the magnitude of $\langle u'u'\rangle$ is much larger than those of $\langle v'v'\rangle$ and $\langle w'w'\rangle$, making the largest contribution to the value of TKE among the three Reynolds normal stress components. Figure 14(*d*) displays the spanwise profile of the Reynolds shear stress $-\langle u'v'\rangle$, which exhibits a similar trend to that for the streamwise Reynolds normal stress $\langle u'u'\rangle$. Owing to the cross-stream secondary flow motion, the profile of $-\langle u'v'\rangle$ peaks in the region between the sidewall and duct centre. Also, as is evident from figure 14, at the same elevation relative to the rib crest, the magnitude of $-\langle u'v'\rangle$ increases with the increase of blockage ratio. In fact, from figures 13 and 14, it is clear that the turbulence level as indicated by the magnitudes of Reynolds normal and shear stresses all increase monotonically as the rib height increases in the central region of the duct.

3.4. *Effect of rib height on non-equilibrium turbulence*

To further understand the impact of the rib height on the turbulence statistics discussed in § 3.3, the vertical profiles of the TKE production rate, $P_k = -\langle u_i'u_j'\rangle \partial\langle u_i\rangle/\partial x_j$, dissipation

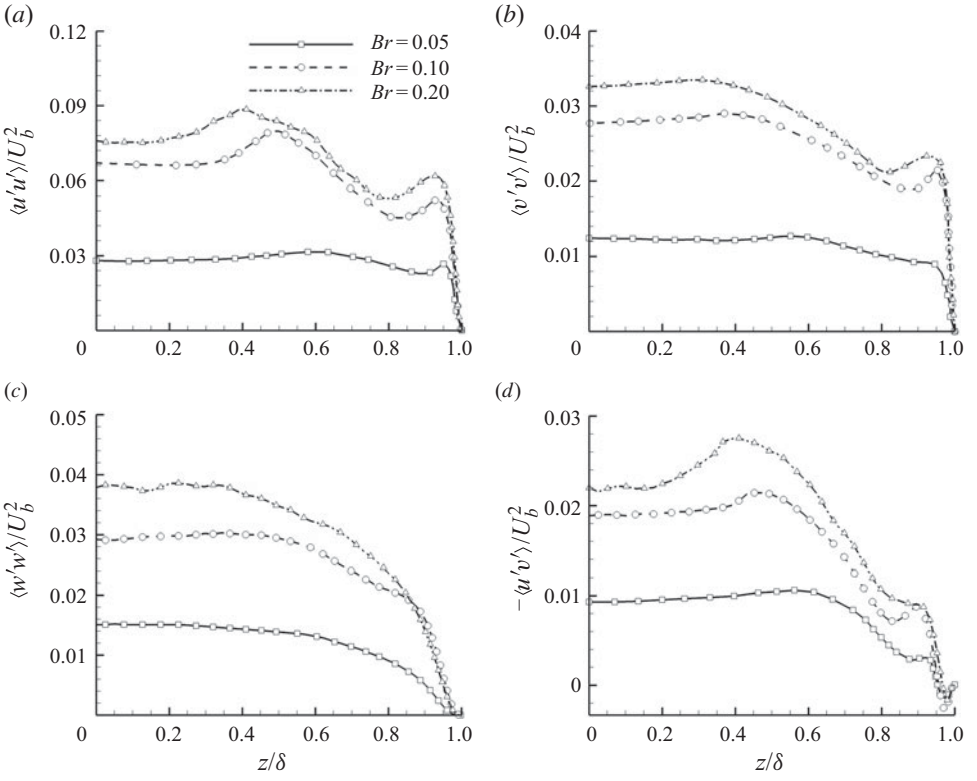

FIGURE 14. Spanwise profiles of Reynolds normal ($\langle u'u'\rangle$, $\langle v'v'\rangle$ and $\langle w'w'\rangle$) and shear ($-\langle u'v'\rangle$) stresses along elevated lines positioned at $(x'/\delta, y/\delta) = (0.4, -0.6)$, $(0.4, -0.5)$ and $(0.4, -0.3)$ for three blockage ratios of $Br = 0.05$, 0.1 and 0.2, respectively. Given the difference in rib heights, these three positions correspond to the same relative elevation that is 0.3δ above the rib crest in each case. Owing to spanwise symmetry, only one half of the duct is plotted. (*a*) Profiles of $\langle u'u'\rangle$, (*b*) profiles of $\langle v'v'\rangle$, (*c*) profiles of $\langle w'w'\rangle$ and (*d*) profiles of $-\langle u'v'\rangle$.

rate, $\varepsilon_k = \nu\langle \partial u_i'/\partial x_j \partial u_i'/\partial x_j\rangle$, and their ratio, P_k/ε_k, are plotted in figure 15 along the same central vertical line as for displaying Reynolds stress profiles in figure 13. From figures 15(*a*) and 15(*b*), it is clear the production rate P_k and dissipation rate ε_k are significantly higher on the ribbed wall side than on the smooth top wall side in all three test cases. The high TKE production and dissipation rates on the ribbed side of the duct are indeed characteristics of this rib-roughened 3-D duct flow, which features strong secondary flows that facilitate transport of TKE in the cross-stream directions. Similar observations were noted by Hirota *et al.* (1992), who conducted LDV measurements of turbulent flows in a square duct with ribs mounted on one wall. Both P_k and ε_k peak around the rib crest, and their magnitude increases monotonically with the Br value. The appearance of this TKE production peak is due to the strong shear layer formed immediately above the rib crest, where the level of the mean spanwise vorticity (i.e. $\langle\omega_z\rangle = \partial\langle v\rangle/\partial x - \partial\langle u\rangle/\partial y$) is significantly augmented. This peak of P_k coincides with that in the Reynolds stress profiles shown previously in figure 13. Furthermore, the presence of ribs in the duct imposes significant inhomogeneities on the turbulence field such that the TKE production rate P_k is not balanced by its dissipation rate ε_k (i.e. $P_k/\varepsilon_k \neq 1$). Figure 15(*c*) compares the ratio of the production to dissipation of TKE along the vertical

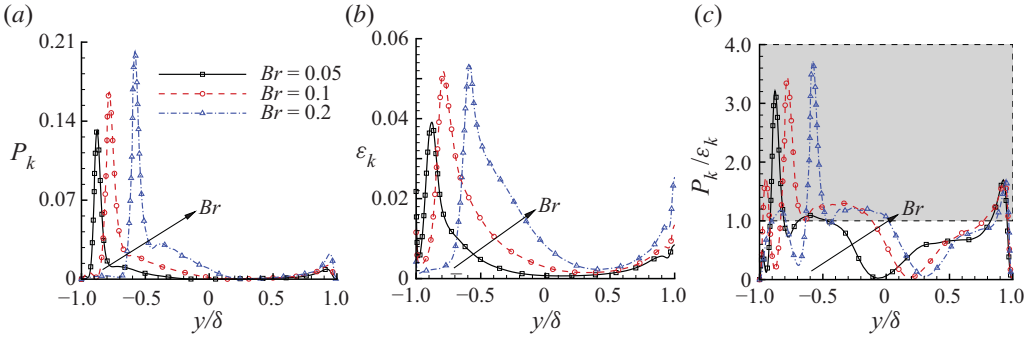

FIGURE 15. Vertical profiles of the TKE production term (P_k), dissipation term (ε_k) and their ratio (P_k/ε_k) along the central vertical line located at $(x'/\delta, z/\delta) = (0.4, 0.0)$ for different blockage ratios. The values of P_k and ε_k are non-dimensionalized using the duct half-height, δ, and bulk velocity, U_b. The grey area shown in panel (c) pertains to the non-equilibrium region in which $P_k/\varepsilon_k > 1$. (a) Profiles of P_k, (b) profiles of ε_k and (c) profiles of P_k/ε_k.

line located at $(x'/\delta, z/\delta) = (0.4, 0.0)$ for the three different rib cases. As shown in this figure, the maximum value of P_k/ε_k occurs slightly above the rib crest, creating a zone of strong non-equilibrium turbulence. Furthermore, as shown in figure 15(c), as the rib height increases, the degree of non-equilibrium as indicated by the peak value of P_k/ε_k increases on the ribbed bottom wall side, but remains invariant on the smooth top wall side. Specifically, close to the rib crest, the rib case with $Br = 0.2$ exhibits a maximum value of P_k/ε_k that is approximately 16 % and 9 % higher than those of $Br = 0.05$ and 0.1, respectively. figure 15(c) also indicates that in all three rib cases, the magnitude of P_k/ε_k decreases significantly upon approaching the duct centre where P_k/ε_k almost vanishes. This reduction is ultimately attributed to the more rapid decrease in the value of P_k compared to the decrease in the value of ε_k in central regions well above the ribs and below the top smooth wall.

figure 16 compares the spanwise profiles of P_k, ε_k and P_k/ε_k for the three rib cases. As is clear in figure 16(a), the profile of P_k exhibits two distinct peaks, one near the sidewall and one distant from the sidewall at approximately $z/\delta = 0.4$. These two peaks reflect the wall-anisotropic effect and the occurrence of the secondary flow pattern in the cross-stream direction demonstrated previously in figure 9, respectively. Consistent with the pattern shown in figures 14(a) and 14(d), turbulence of high-level TKE and TKE production rate is convected towards the ribbed wall due to the increasingly stronger secondary flow as the blockage ratio increases from $Br = 0.05$ to 0.2. By contrast, as shown in figure 17(b), although the magnitude of the dissipation rate ε_k increases as the Br value increases, it is less sensitive to the rib height, especially in the central region of the channel. Consequently, the profile of P_k/ε_k displayed in figure 17(c) exhibits a similar trend to that of P_k. From figure 17(c), it is also seen that the value of P_k/ε deviates from unity on most occasions at all three rib cases, which is a clear indication of non-equilibrium turbulence characteristic of a ribbed duct flow.

3.5. *Effect of rib height on TKE budget*

To further understand the rib effects on turbulence energy transfer in the vertical direction, the transport equation of TKE (defined as $k = \langle u_i' u_i' \rangle / 2$) for a statistically stationary flow

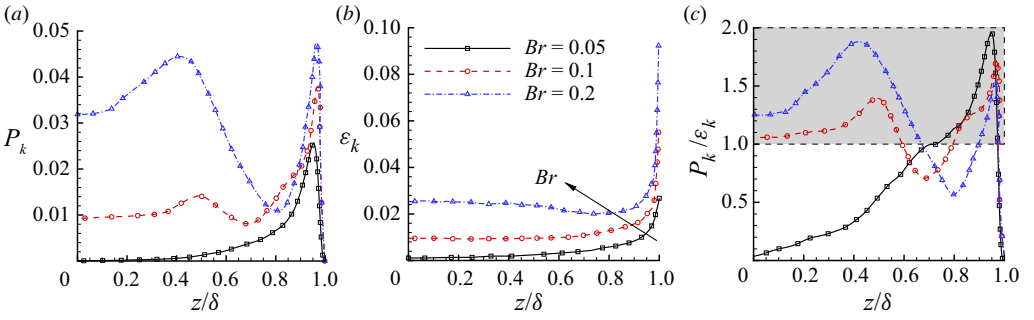

FIGURE 16. Spanwise profiles of the TKE production term (P_k), dissipation term (ε_k) and their ratio (P_k/ε_k) along elevated lines positioned at $(x'/\delta, y/\delta) = (0.4, -0.6)$, $(0.4, -0.5)$ and $(0.4, -0.3)$ for three blockage ratios of $Br = 0.05$, 0.1 and 0.2, respectively. Given the difference in rib heights, these three positions correspond to the same relative elevation that is 0.3δ above the rib crest in each case. Owing to spanwise symmetry, only one half of the duct is plotted. The values of P_k and ε_k are non-dimensionalized using the duct half-height, δ, and bulk velocity, U_b. The grey area shown in panel (*c*) pertains to the non-equilibrium region in which $P_k/\varepsilon_k > 1$. (*a*) Profiles of P_k, (*b*) profiles of ε_k and (*c*) profiles of P_k/ε_k.

can be studied, which reads as

$$\underbrace{\langle u_j\rangle \frac{\partial k}{\partial x_j}}_{C_k} = \underbrace{-\frac{1}{\rho}\frac{\partial \langle p' u_j'\rangle}{\partial x_j}}_{\Pi_k} \underbrace{-\frac{1}{2}\frac{\partial \langle u_i' u_i' u_j'\rangle}{\partial x_j}}_{T_k} + \underbrace{\nu \frac{\partial^2 k}{\partial x_j^2}}_{D_k} \underbrace{-\langle u_i' u_j'\rangle \frac{\partial \langle u_i\rangle}{\partial x_j}}_{P_k} \underbrace{-\nu \left\langle \frac{\partial u_i'}{\partial x_j}\frac{\partial u_i'}{\partial x_j}\right\rangle}_{\varepsilon_k}, \tag{3.1}$$

where C_k, Π_k, T_k and D_k represent the convection, pressure diffusion, turbulent diffusion and viscous diffusion, respectively. Figure 17 shows the vertical profiles of the budget terms of TKE along the central vertical line positioned at $(x'/\delta, z/\delta) = (0.4, 0.0)$ for the smooth duct case and all three rib cases. The profiles of the TKE budget terms of the smooth square duct flow are plotted in figure 17(*a*), which shows that the budget balance of TKE is dominated by viscous diffusion T_k and viscous dissipation ε_k in the vicinity of the wall as the source and sink terms, respectively. The turbulent diffusion term T_k is zero at the wall, becomes positively valued in the vicinity of the wall (for $y/\delta < -0.95$), and then changes its sign and reaches its negatively valued peak at $y/\delta = -0.9$. At this elevation $y/\delta = -0.9$, the primary source of TKE is the production term P_k, which is mainly balanced by three sinks, i.e. viscous dissipation ε, viscous diffusion D_k and turbulent diffusion T_k. As the duct centre is approached, the magnitudes of all budget terms diminish, although the balance is primarily between P_k and ε (which are almost mirror images of each other). The characteristics of the TKE budget terms analysed here are consistent with those of Vinuesa *et al.* (2014), who conducted a DNS study of duct flows at a similar Reynolds number.

By comparing figure 17(*b–d*) with 17(*a*), it is apparent that the budget balances of the three rib cases exhibit more complex patterns than that of the smooth duct flow, especially around the rib crest. Furthermore, owing to the fact the vertical profiles of the budget terms are asymmetrical in the vertical direction due to the presence of ribs, the entire vertical profiles between the ribbed and smooth walls need to be plotted in figure 17(*b–d*). In comparison with the smooth duct flow, the dominant source term is still the production term P_k, which peaks at a position that is slightly above rib crest in all three rib cases (as

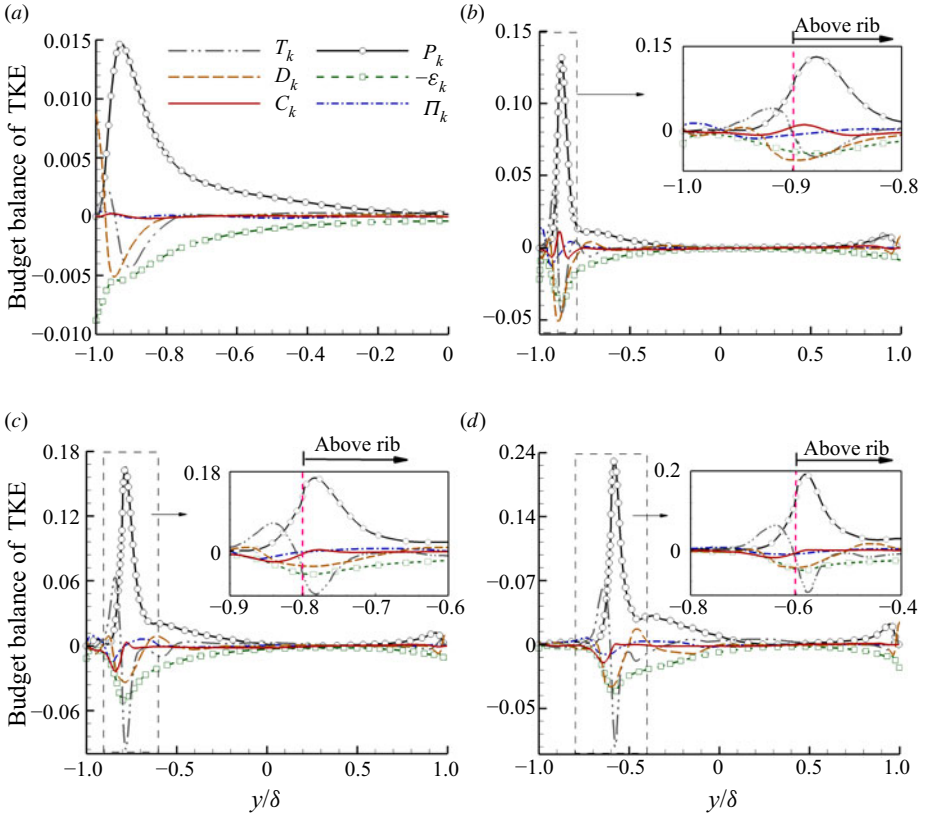

FIGURE 17. Vertical profiles of budget terms of the TKE transport equation along the vertical line positioned at $(x'/\delta, z/\delta) = (0.4, 0.0)$ for the smooth duct flow and three ribbed duct flows of different blockage ratios. The budget terms are non-dimensionalized using the duct half-height, δ, and bulk velocity, U_b. In panel (a), for the smooth duct case, only one-half the duct is plotted due to vertical symmetry. For the three rib duct cases, in order to show clearly the profiles of the budget terms around the rib crest, they are partially enlarged and replotted in inset graphs in panels (b)–(d). The vertical pink dashed line demarcates the rib crest in the inset graphs. (a) Smooth duct, (b) $Br = 0.05$, (c) $Br = 0.1$, and (d) $Br = 0.2$.

shown in the inset graphs). By comparing figure 17$(b$–$d)$, it is seen that the magnitudes of the three sinks (D_k, T_k and ε) around the rib crest are comparable at $Br = 0.05$; however, the turbulent diffusion term T_k becomes increasingly dominant as the blockage ratio increases to $Br = 0.1$ and 0.2. By comparing the three rib cases with the smooth duct case, it is observed that the convection of TKE by the mean flow is vanishingly small as the convention term C_k does not make a remarkable contribution to the budget balance of TKE in the smooth duct flow. By contrast, as shown in figure 17$(b$–$d)$, the effect of the convection term C_k becomes more pronounced due to the complex mean flow pattern and high TKE level around the rib crest in all three rib cases. From figure 17$(b$–$d)$, it is clear that the magnitudes of the budget terms are much larger on the ribbed bottom wall side than on the smooth top wall side. A careful perusal of figure 17$(b$–$d)$ further indicates that the profile patterns of the budget terms on the smooth top wall side are, actually, similar to those of the smooth duct flow shown in figure 17(a).

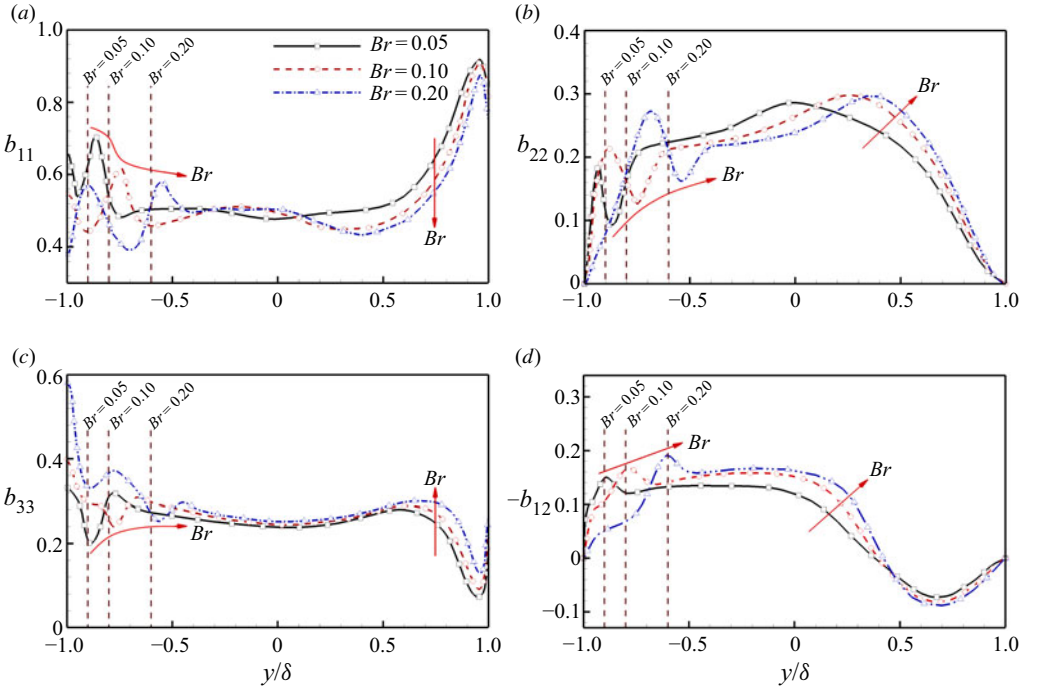

FIGURE 18. Vertical profiles of Reynolds stress anisotropy tensor components (b_{11}, b_{22}, b_{33} and $-b_{12}$) along the central vertical line positioned at $(x'/\delta, z/\delta) = (0.4, 0.0)$ for different blockage ratios. The vertical dashed lines demarcate the rib crests for test cases of $Br = 0.05$, 0.1 and 0.2. The red arrow shows the trend of how the value of b_{ij} varies monotonically with an increasing Br value. (*a*) Profiles of b_{11}, (*b*) profiles of b_{22}, (*c*) profiles of b_{33} and (*d*) profiles of $-b_{12}$.

3.6. *Effect of rib height on turbulence anisotropy*

The effects of rib height on turbulence anisotropy can be studied through the Reynolds stress anisotropy tensor, defined as (Pope 2000)

$$b_{ij} = \frac{\langle u_i' u_j' \rangle}{\langle u_k' u_k' \rangle} - \frac{1}{3}\delta_{ij}. \tag{3.2}$$

Previous studies of turbulence anisotropy in 2-D turbulent plane-channel flows with surface-mounted perpendicular ribs (Krogstad & Antonia 1994; Keirsbulck *et al.* 2002; Krogstad *et al.* 2005) showed that the anisotropic states of turbulence become less apparent near the rough wall. However, Mazouz, Labraga & Tournier (1998) showed that the degree of anisotropy enhances with the use of *k*-type surface roughness in a 3-D duct flow. These results indicate that turbulence anisotropy varies with not only roughness configurations but also the 2-D or 3-D flow conditions. The profiles of the Reynolds stress anisotropy tensor components (b_{11}, b_{22}, b_{33} and $-b_{12}$) are plotted in figure 18 for all three rib cases along the central vertical line positioned at $(x'/\delta, z/\delta) = (0.4, 0.0)$. To facilitate our study of the rib height effect on the flows, the position of the rib crest is demarcated using a vertical dashed line in figure 18 for each rib case. By comparing figure 18(*a–c*), it is observed that the value of b_{11} is larger than those of b_{22} and b_{33} in the region between the rib crest and the smooth top wall ($y/\delta = 1.0$), which is a clear indication of turbulence anisotropy. From figure 18(*a*), it is evident that the value of b_{11} peaks immediately above

the rib crest whose magnitude decreases monotonically as the blockage ratio increases from $Br = 0.05$ to 0.2. Because the value of b_{11} is larger than those of b_{22} and b_{33} in the region immediately above the rib crest, a reduction in the peak value of b_{11} with Br reduces the degree of turbulence anisotropy. This can be further understood from figures 12 and 13, which show that as the rib height increases, the strength of induced disturbances by the rib elements increases, making turbulence more isotropic. From figure 18(*a*), it is seen that the magnitude of b_{11} reaches its maximum near the smooth top wall ($y/\delta = 1.0$) in all the three rib cases. This is consistent with the observation of the near-wall peak value of $\langle u'u' \rangle$ on the smooth top wall side shown previously in figure 13(*a*). The wall anisotropy as represented by the peak values of b_{11} and $\langle u'u' \rangle$ near the smooth top wall is similar to those of a smooth plane-channel flow observed by Kim *et al.* (1987) and Lamballais, Lesieur & Métais (1997).

From figure 18(*a–c*), it is clear that on the smooth top wall side, the value of b_{11} decreases monotonically with an increasing value of Br; however, those of b_{22} and b_{33} increase monotonically. These trends reflect the fact that as the rib height increases, the flow becomes more disturbed by the rib elements. The highly disturbed turbulence generated around the rib crest spreads to the smooth top wall side of the duct through mechanisms such as vortex shedding and secondary flows. As such, TKE is more evenly distributed among the three normal components, which leads to a decrease in the degree of turbulence anisotropy. From figure 18(*d*), it is observed that similar to the trends of b_{22} and b_{33}, the value of $-b_{12}$ increases monotonically as the rib height increases from $Br = 0.05$ to 0.2 in the region immediately above the rib crest. This phenomenon is strongly associated with the enhanced strength of the shear layer developed over the rib crest.

In order to study the effect of rib height on small-scale turbulence anisotropy, the following anisotropy tensor of the dissipation rate can be calculated (Speziale & Gatski 1997):

$$d_{ij} = \frac{\varepsilon_{ij}}{2\varepsilon_k} - \frac{1}{3}\delta_{ij}. \tag{3.3}$$

Here ε_{ij} represents the dissipation tensor, defined as

$$\varepsilon_{ij} = 2\nu \left\langle \frac{\partial u_i'}{\partial x_k} \frac{\partial u_j'}{\partial x_k} \right\rangle. \tag{3.4}$$

Figure 19 displays the vertical profiles of the dissipation anisotropy tensor components (d_{11}, d_{22}, d_{33} and $-d_{12}$) along the central vertical line positioned at $(x'/\delta, z/\delta) = (0.4, 0.0)$. From figure 19(*a*), it is clear that, for all three rib cases, the magnitude of d_{11} peaks around the rib crest, which decreases monotonically as the rib height increases. By comparing figures 19 and 18, it is observed that the profiles of d_{ij} feature a similar shape to that of b_{ij}, especially in terms of their peak positions around the rib crest and trends on the smooth top wall side. This is not surprising from the point of view of energy conservation, as the strength of the local TKE dissipation rate is often consistent with that of local TKE and TKE production rate. In fact, from the point of view of spectral analysis, the TKE dissipation rate is dominated by small scales of turbulence, and by contrast, the magnitude of Reynolds stresses is dominated by relatively large scales characteristic of the most energetic eddies. Therefore, a similar pattern between b_{ij} and d_{ij} indicates that the rib elements in the square duct have a profound influence on both the small- and large-scale structures in terms of their reflections of the degree of local turbulence anisotropy. From figure 19(*a–c*), it is seen that the magnitude of d_{11} is larger than those of d_{22} and d_{33}

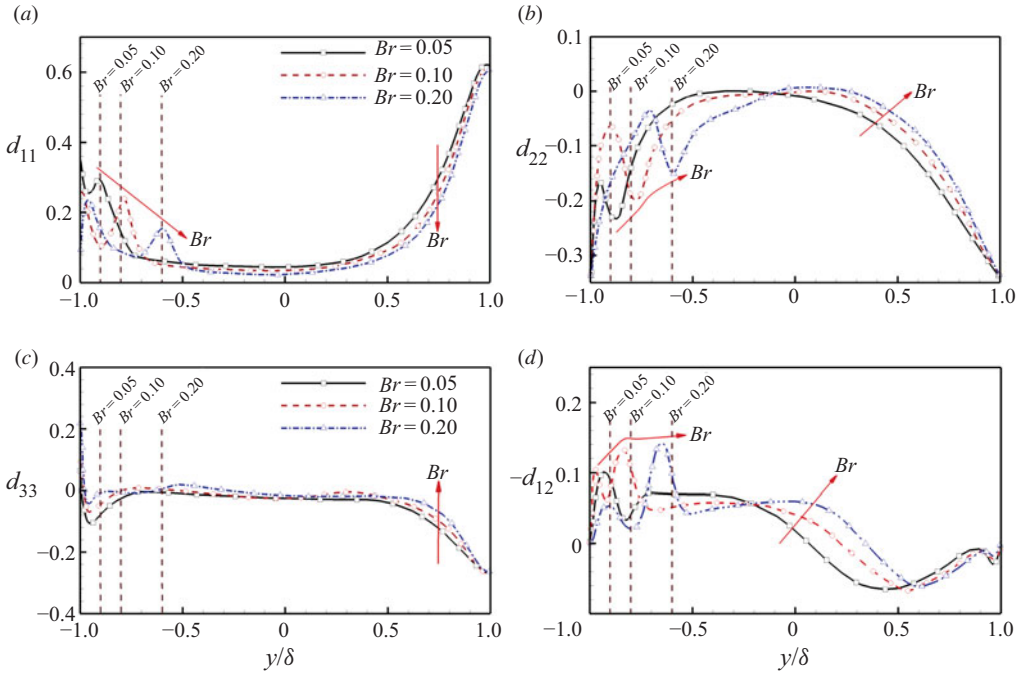

FIGURE 19. Vertical profiles of the anisotropy of the Reynolds stress dissipation rate (d_{11}, d_{22}, d_{33} and $-d_{12}$) tensors along the central vertical line positioned at $(x'/\delta, z/\delta) = (0.4, 0.0)$ for different blockage ratios. The vertical dashed lines demarcate the rib crests for test cases of $Br =$ 0.05, 0.1 and 0.2. The red arrow shows the trend of how the value of d_{ij} varies monotonically with an increasing Br value. (*a*) Profiles of d_{11}, (*b*) profiles of d_{22}, (*c*) profiles of d_{33} and (*d*) profiles of $-d_{12}$.

around the rib crest. Furthermore, from figures 19(*a*) and 19(*b*), it is evident that as the Br value increases, the peak value around the rib crest decreases monotonically for d_{11} but increases monotonically for d_{22}. This helps to reduce the differences between the magnitudes of d_{11}, d_{22} and d_{33}, and therefore reducing the degree of turbulence anisotropy. From figure 19(*a–c*), it is interesting to observe that the magnitudes of the normal components of the dissipation anisotropy tensor, d_{11}, d_{22} and d_{33}, are close to zero in the duct centre for $-0.5 < y/\delta < 0.5$. By contrast, as shown in figure 18(*a–c*), the values of the normal components of the Reynolds stress anisotropy tensor, b_{11}, b_{22} and b_{33} deviate apparently from zero in the same region. This indicates that small-scale structures exhibit a stronger 'return to isotropy' tendency compared to the large scales in the duct centre. As is clear from figure 19(*d*), similar to the trend of $-b_{12}$ shown in figure 18(*d*), the anisotropy of the dissipation rate tensor component $-d_{12}$ peaks around the rib crest for all three Br numbers tested. Furthermore, the peak value increases monotonically as the rib aspect ratio increases from $Br = 0.05$ to 0.2, suggesting an increase of TKE dissipation at small scales due to the shear layer generated by the rib elements.

3.7. *Third-order moments of velocity fluctuations and quadrant analysis*

It is well established (Andreopoulos & Bradshaw 1981; Krogstad & Antonia 1999; Hurther, Lemmin & Terray 2007) that turbulent transport of TKE can be better elucidated by examining velocity triple correlations as compared to the second-order

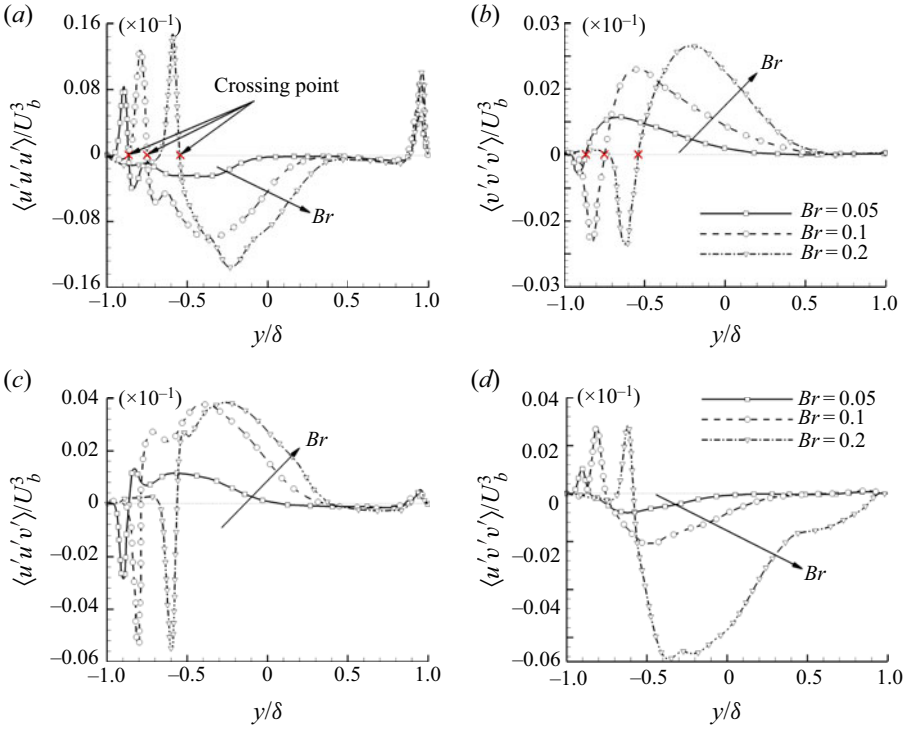

FIGURE 20. Vertical profiles of $\langle u'u'u'\rangle$, $\langle v'v'v'\rangle$, $\langle u'u'v'\rangle$ and $\langle u'v'v'\rangle$ along the central vertical line positioned at $(x'/\delta, z/\delta) = (0.4, 0.0)$ for different blockage ratios. The crossing points are marked using a red cross symbol '×', where $\langle u'u'u'\rangle = 0$ and $\langle v'v'v'\rangle = 0$ (in particular, when the sign of $\langle u'u'u'\rangle$ changes from positive to negative and the sign of $\langle v'v'v'\rangle$ changes from negative to positive). The crossing point occurs at elevation of $y/\delta = -0.88$, -0.78 and -0.58 for $Br = 0.05$, 0.1 and 0.2, respectively. (*a*) Profiles of $\langle u'u'u'\rangle$, (*b*) profiles of $\langle v'v'v'\rangle$, (*c*) profiles of $\langle u'u'v'\rangle$ and (*d*) profiles of $\langle u'v'v'\rangle$.

statistical moments. For instance, Hurther *et al.* (2007) measured TKE fluxes in a rough-wall open channel flow using an acoustic Doppler velocity profiler. They reported that high-order statistical moments of the flow are highly sensitive to the wall roughness in both the inner and outer regions of the boundary layer, and the difference between the production and dissipation rates in the rough-wall region is responsible for the intensification of TKE fluxes. In this part of the study, our attention is paid to the influence of rib height on the third-order statistics and the crossing point between ejections and sweeps, where the signs of $\langle u'u'u'\rangle$ and $\langle v'v'v'\rangle$ change in the vertical direction.

In figure 20 the non-dimensional vertical profiles of fluctuating velocity triple product components $\langle u'u'u'\rangle/U_b^3$, $\langle v'v'v'\rangle/U_b^3$, $\langle u'u'v'\rangle/U_b^3$ and $\langle u'v'v'\rangle/U_b^3$ are plotted along the central vertical line located at $(x'/\delta, z/\delta) = (0.4, 0.0)$ for three rib cases. Figures 20(*a*) and 20(*b*) show the progressive enhancement of both $\langle u'u'u'\rangle$ and $\langle v'v'v'\rangle$ in the vicinity of the rib crest as the rib height increases. This enhancement of triple correlations results in a delayed appearance of the crossing point in the sense that it occurs at a higher elevation as the rib height increases. In figures 20(*a*) and 20(*b*) the crossing points are marked using a red cross symbol '×', where $\langle u'u'u'\rangle = 0$ and $\langle v'v'v'\rangle = 0$ (in particular, where the sign of $\langle u'u'u'\rangle$ changes from positive to negative and the sign of $\langle v'v'v'\rangle$ changes from negative to positive). The crossing point occurs at elevations of $y/\delta = -0.88$, -0.78

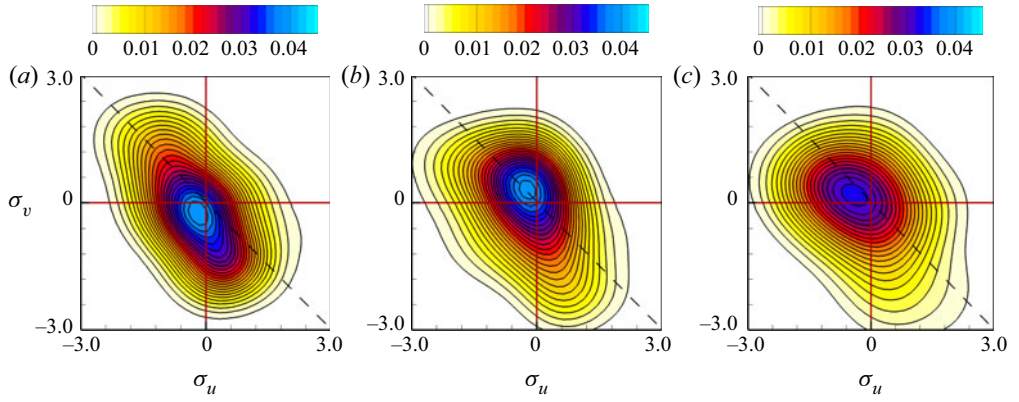

FIGURE 21. Contours of JPDF of σ_u and σ_v of the smooth square duct flow at three elevated points along the central vertical line located at $z/\delta = 0.0$. Corresponding to panels (a), (b) and (c), the elevation is $y/\delta = -0.95$, -0.9 and -0.8, respectively.

and -0.58 for $Br = 0.05$, 0.1 and 0.2, respectively. In the region near the rib crest below the crossing point, positive-valued peaks of $\langle u'u'u' \rangle$ clearly demonstrate the occurrence of high-speed streaks, which are reinforced as the rib height increases. Furthermore, as seen in figures 20(a) and 20(b), the values of $\langle u'u'u' \rangle$ and $\langle v'v'v' \rangle$ are positive and negative near the rib crest, respectively, which clearly indicate that the turbulent flow is strongly influenced by the flapping motions of the shear layer, leading to enhanced sweeping activities. In consequence, a considerable amount of high momentum fluid is swept into the inter-rib region (below the rib height). By contrast, in the region above the crossing point, the trends of $\langle u'u'u' \rangle$ and $\langle v'v'v' \rangle$ are entirely opposite, and an enhancement of the ejection mechanism is observed. This results in enhanced transport of low-momentum fluids towards the upper half of the duct due to the existence of local spanwise swirling motions. This observation is consistent with the results of Keirsbulck *et al.* (2002) who studied the 2-D turbulent boundary layer over a k-type rough wall using PIV measurements. Because $\langle u'u'v' \rangle$ and $\langle u'v'v' \rangle$ dominate the other turbulent diffusion terms, only the vertical turbulent transports of $\langle u'u' \rangle$ and $\langle u'v' \rangle$ (embodied by the profiles of $\langle u'u'v' \rangle$ and $\langle u'v'v' \rangle$) are shown in figures 20(c) and 20(d), respectively. As shown in figure 20(c), $\langle u'u'v' \rangle$ is negatively valued below the crossing point. Therefore, there exists a strong turbulent diffusion of energy (or vertical flux of $\langle u'u' \rangle$) towards the bottom wall near the rib crest with a streamwise acceleration (owing to the positive sign of $\langle u'u'u' \rangle$). By contrast, above the crossing point, the sign of $\langle u'u'v' \rangle$ switches from negative to positive, indicating the turbulent diffusion is outwards with a streamwise deceleration due to the negative values of $\langle u'u'u' \rangle$. On the opposite trend of $\langle u'u'v' \rangle$, figure 20(d) shows that the magnitude of $\langle u'v'v' \rangle$ increases and a positively valued peak occurs near the rib crest due to enhanced sweep motions. However, the value of $\langle u'v'v' \rangle$ switches its sign from positive to negative in the region above the rib crest, associated with a strong outward flux of $\langle u'v' \rangle$ due to enhanced ejection motions.

To further understand the effects of rib height on Reynolds stresses, the JPDF of $\sigma_u = u'/u_{rms}$ and $\sigma_v = v'/v_{rms}$ is calculated in the central vertical line located at $(x'/\delta, z/\delta) = (0.4, 0.0)$. The JPDF of σ_u and σ_v for the smooth duct flow is used as a baseline comparison case, which is shown in figure 21, and those of the three ribbed duct flows are displayed in figure 22. Three different elevations (of $y/\delta = -0.95$, -0.9 and -0.8) are compared for each case of the smooth and ribbed duct flows. The choice

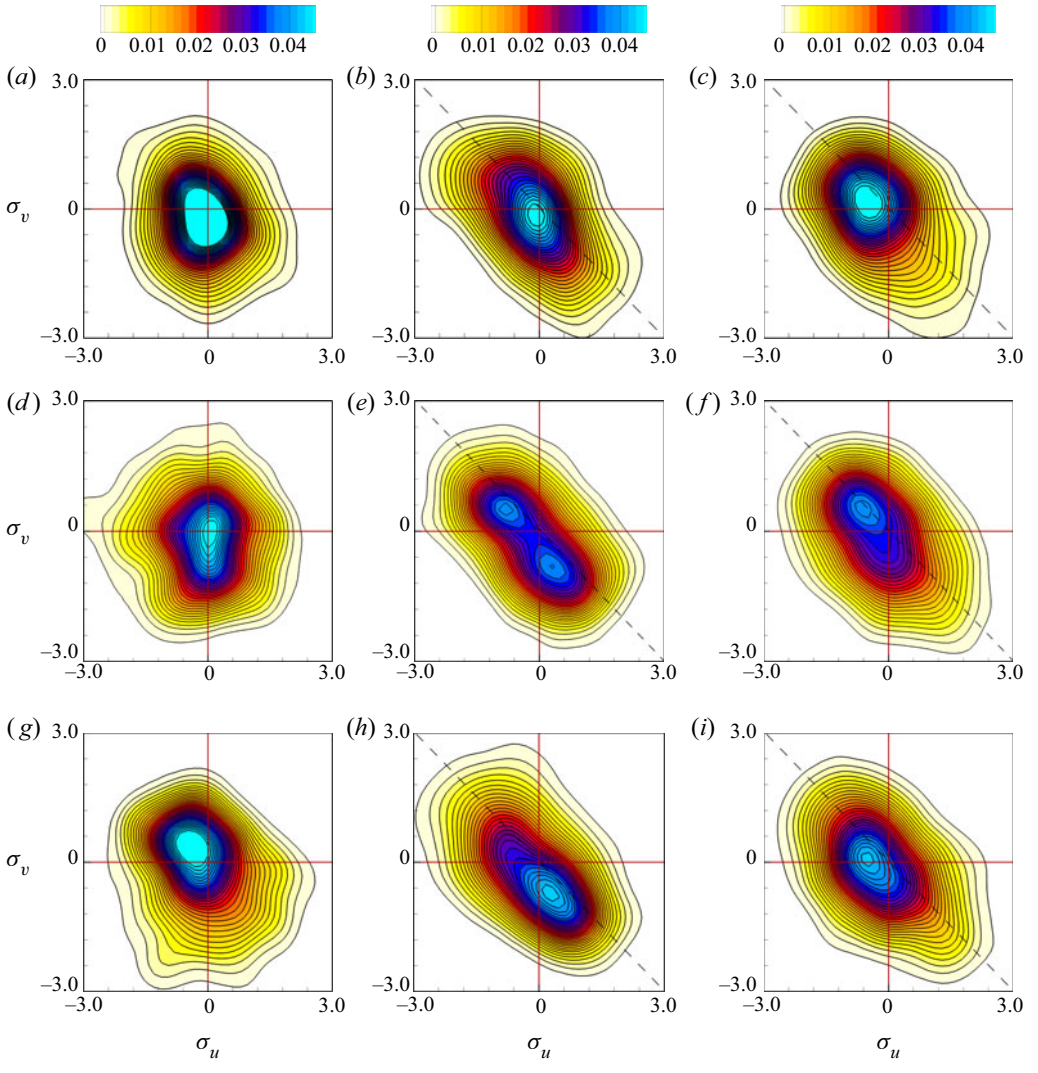

FIGURE 22. Contours of JPDF of σ_u and σ_v at three elevated points along the central vertical line located at $(x'/\delta, z/\delta) = (0.4, 0.0)$ for three different blockage ratios. The elevated points are located at the mid height of the rib, immediately above the rib crest, and above the crossing point for each test case of a specific blockage ratio. In panels (a), (b) and (c), the elevation is $y/\delta = -0.95, -0.86, -0.4$ for $Br = 0.05$; in panels (d), (e) and (f), the elevation is $y/\delta = -0.9, -0.76, -0.4$ for $Br = 0.1$; and in panels (g), (h) and (i), the elevation is $y/\delta = -0.8, -0.56, -0.4$ for $Br = 0.2$.

of these three elevations of the smooth duct is not arbitrary, as they correspond to the mid height of the rib in three ribbed ducts of $Br = 0.05$, 0.1 and 0.2. From figure 21, it is seen that the streamwise velocity fluctuations synchronize well with the vertical velocity fluctuations in all three elevations, as the plotted JPDF patterns exhibit a tendency to be aligned approximately at 135° throughout quadrants II and IV (i.e. 'Q2' and 'Q4', respectively). This indicates a preference for the ejection events (featuring $u' < 0$ and $v' > 0$ associated with Q2) and sweeping events (featuring $u' > 0$ and $v' < 0$ associated with Q4) at all three elevations near the bottom wall. The explanation for this preference

is a well-known conclusion of the classical boundary-layer theory. According to Adrian (2007), Reynolds stress $-\langle u'v'\rangle$ is positively valued in the near-wall region due to the dominance of the ejection and sweep events.

By comparing figure 22 with 21, it is clear that there are differences between the JPDF patterns of the three rib cases and those of the smooth duct flow. In order to facilitate a fair comparison between the smooth and ribbed duct flows, the JPDFs in figures 22(*a*), 22(*d*) and 22(*g*) are calculated at the mid-rib height in each ribbed duct case (at $y/\delta = -0.95$, -0.9 and -0.8, respectively). These three elevations are exactly the same as those for figure 21(*a–c*) for the smooth duct flow. By comparing figures 22(*a*) and 22(*d*) with 21(*a*) and 21(*b*), respectively, it is clear that both ejection and sweeping motions are significantly reduced at the mid height of the ribs in ribbed duct flow cases $Br = 0.05$ and 0.1. This indicates that the distribution and intensity of the JPDF is approximately identical for each quadrant at the mid-rib height, where u' and v' are essentially uncorrelated, causing arbitrary occurrence of either ejection or sweeping events with no obvious directional tendency. However, for the $Br = 0.2$ case, as shown in figure 22(*g*), the tendency towards ejection motion is observed at the mid-rib height. As shown in figures 22(*b*), 22(*e*) and 22(*h*), near the rib crest, it is observed that the sweep and ejection events are dominant, which are mainly attributed to the large-scale flapping motions in this region. Consistent with the quadrant analysis of Reynolds shear stresses reviewed by Adrian (2007), these turbulent motions associated with the Q2 and Q4 events result in a negatively valued Reynolds shear stress $\langle u'v'\rangle$ close to the rib crest (see figure 13*d*). The thick black dashed line at the 135° angle indicates a high correlation between components at the reference point. Figures 22(*c*), 22(*f*) and 22(*i*) show that in the region above the crossing point ($y/\delta = -0.4$), the JPDF distribution prefers the Q2 events. This turbulent flow is strongly influenced by the presence of unsteady large-scale swirling flow structures, which lead to an augmentation of ejection activities.

4. Flow structures near the rib-roughened wall

The presence of ribs and four walls has a significant impact on the turbulent flow statistics and structures. In this section we focus on the study of turbulent structures through a qualitative approach based on visualizations using the instantaneous fluctuating flow field and the λ_{ci}-criterion, and through a quantitative approach based on analysis of temporal auto-correlations, temporal spectra and the spatial two-point auto-correlations of the turbulence field.

4.1. *Turbulence structures in the x–y plane*

In order to demonstrate the effect of ribs on near-wall turbulence structures, figure 23 shows the isosurfaces of the swirling strength, λ_{ci}, superimposed onto instantaneous vertical velocity contours in the central x–y plane (located at $z/\delta = 0.0$) for different blockage ratios. From figure 23, it is clear that both the strength and size of turbulent structures induced by rib elements increase as the rib height increases, an observation that is consistent with the pattern of turbulence fluctuations shown in figure 12 and the trend of TKE production rate P_k demonstrated in figure 15(*a*). As the rib height increases, the sweeping or ejection activities ('splashing effects') near the leading corner of the rib element enhance, which drastically deflect the vortical structures away from the ribs, shedding into the central region of the duct. This further results in an enhancement in the local Reynolds normal and shear stress levels and TKE production rate. This physical feature is also consistent with the previous analysis of figures 18 and 19, in the sense that

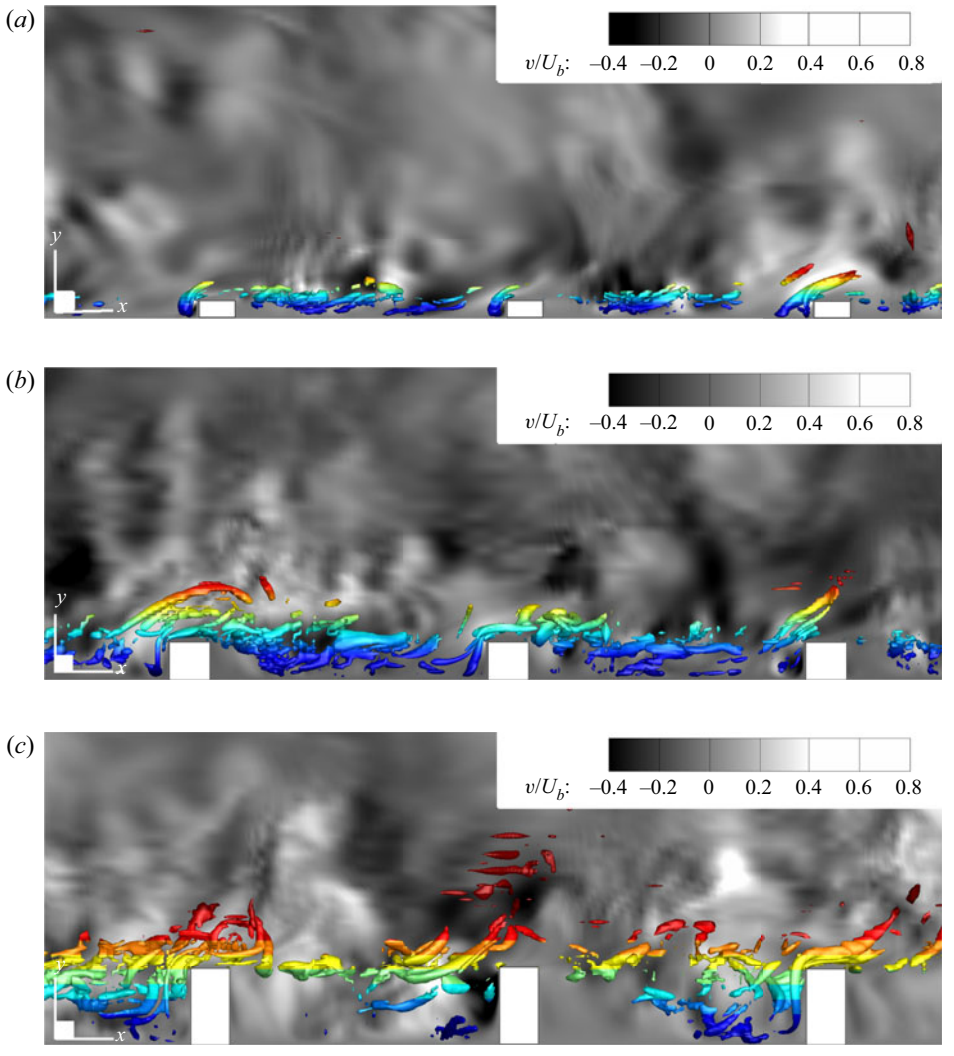

FIGURE 23. Isosurfaces of the swirling strength λ_{ci} around ribs, coloured with non-dimensional elevation y/δ, with background contours of the instantaneous vertical velocity v/U_b in the central vertical plane (located at $z/\delta = 0$) of the domain for three blockage ratios. (*a*) $Br = 0.05$, (*b*) $Br = 0.1$ and (*c*) $Br = 0.2$.

the local isotropy for both large- and small-scales of turbulence near the rib crest becomes increasingly apparent as the blockage ratio increases from $Br = 0.05$ to 0.2.

To develop a deeper understanding of the effect of rib height on the size and inclination angle α of turbulence structures near the rib crest, the 2-D spatial two-point auto-correlation function of velocity fluctuations can be studied. For a ribbed flow, it is defined as (Volino *et al.* 2009)

$$R^s_{ij}(x'_{ref}, y_{ref}, x', y) = \frac{\langle u'_i(x', y) u'_j(x'_{ref}, y_{ref})\rangle}{\sqrt{\langle u'^2_i(x', y)\rangle \langle u'^2_j(x'_{ref}, y_{ref})\rangle}}, \tag{4.1}$$

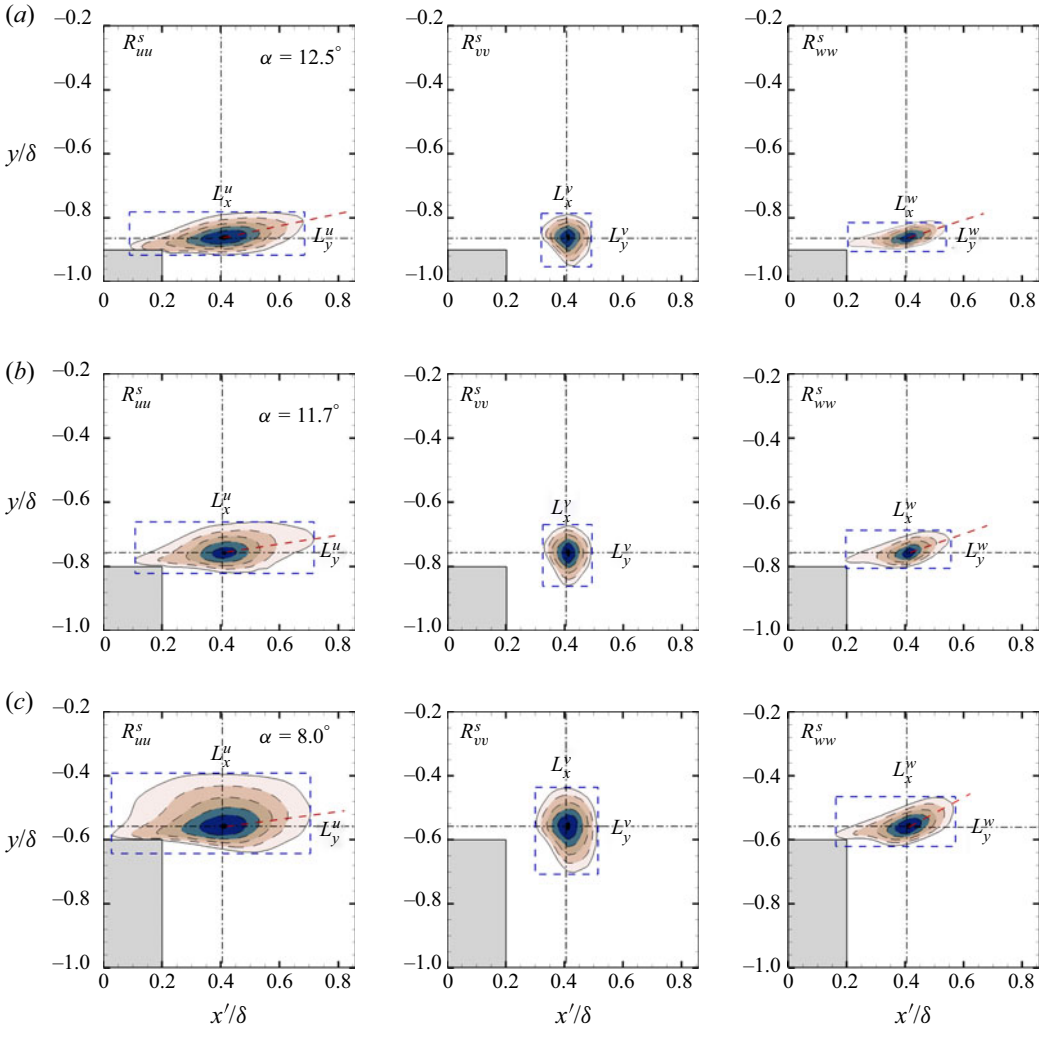

FIGURE 24. Isopleths of two-point auto-correlation $R^s_{ii}(x'/\delta,\, y/\delta)$ of three velocity components displayed in the central vertical plane located at $z/\delta = 0$ for different blockage ratios. The relative streamwise coordinate of the reference point is fixed at $x'_{ref}/\delta = 0.4$, while the vertical coordinate of the reference point is $y_{ref}/\delta = -0.86$, -0.76 and -0.56 for $Br = 0.05$, 0.1 and 0.2, respectively. The isopleth value ranges from 0.5 to 1.0, with the outermost and innermost isopleths corresponding to $R^s_{ii} = 0.5$ and 1.0, respectively. The increment between two adjacent isopleths is 0.1 for all three rib cases. The dashed box contains exactly the outermost isopleth, with side lengths of L^u_x and L^u_y for R^u_{ii}, L^v_x and L^v_y for R^v_{ii}, and L^w_x and L^w_y for R^w_{ii}. (*a*) $Br = 0.05$, (*b*) $Br = 0.1$ and (*c*) $Br = 0.2$.

where $(x'_{ref},\, y_{ref})$ are the coordinates of the reference point and the superscript 's' denotes a spatial correlation. The relative streamwise coordinate of the reference point is fixed at $x'_{ref}/\delta = 0.4$, while its vertical coordinate y_{ref}/δ is determined based on the peak locations of the two Reynolds stress components $\langle u'u' \rangle$ and $-\langle u'v' \rangle$ observed in figure 13, both of which occur at elevations $y/\delta = -0.86$, -0.76 and -0.56 for $Br = 0.05, 0.1$ and 0.2, respectively. Figure 24 plots the isopleths of the spatial two-point auto-correlation

coefficients of the three velocity components (R^s_{uu}, R^s_{vv} and R^s_{ww}) for the three rib cases. As clearly shown in the figure, there is an inclination angle between the tilted major axis of the isopleths and the streamwise direction. This observation is consistent with the study of 2-D turbulent boundary-layer flows over ribbed flat plates of Leonardi *et al.* (2004) and Volino *et al.* (2009), who indicated that this inclination angle is characteristic of hairpin vortices developed over the rib crest. From figure 24, it is evident that the inclination angle of the isopleths of R^s_{uu} decreases monotonically from $\alpha = 12.5^\circ$ to 8.0° as the rib height increases. This physical feature can be explained on the basis that the hairpin vortices are rotated towards the streamwise and vertical directions by the asymmetric part of the shear stress tensor and the self-induction of quasi-streamwise vortices (or hairpin legs) associated with the ejection events (Adrian, Meinhart & Tomkins 2000). Indeed, from the previous analysis of figures 22(*b*), 22(*e*) and 22(*h*), it is understood that as the rib height increases, the flow becomes increasingly dominated by the sweep events around the rib height. As such, along with the relative reduction in the strength of ejection events, the inclination angle decreases. To demonstrate the rib height effects on the size of hairpin structures, we compare the streamwise and vertical length scales of the outermost isopleth of the spatial two-point correlation coefficients (R^s_{uu}, R^s_{vv} and R^s_{ww}), indicated using the side lengths of dashed boxes in figure 24. By comparing figure 24(*a–c*), it is evident that as the rib height increases, both L^u_x and L^u_y (associated with R^s_{uu}) increase in value. This indicates that both the hairpin structures and streamwise streaks appearing near the rib crest increase in size with an increasing rib height. Similar to the isopleth pattern of R^s_{uu}, the major axis of the isopleth of R^s_{ww} also exhibits an inclined angle near the rib crest. Also similar to R^s_{uu}, the streamwise and vertical length scales (L^w_x and L^w_y, respectively) of the outermost isopleth of R^s_{ww} increase as the rib height increases. Although the three spatial two-point auto-correlation coefficients R^s_{uu}, R^s_{vv} and R^s_{ww} are closely related, all influenced by the turbulence structures at the rib crest, they are different in values. From figure 24, it is apparent that in all three rib cases, the extent of the isopleth of R^s_{uu} is greater than those of R^s_{vv} and R^s_{ww}, suggesting that the high- and low-speed streamwise streaks associated with the hairpin legs are the dominant flow structural features around the rib crest. Furthermore, in comparison with R^s_{uu} and R^s_{ww}, the isopleths of R^s_{vv} show a more isotropic distribution. Clearly, the streamwise and vertical length scales of the turbulent flow structures as indicated by the outermost isopleth of R^s_{vv}, L^v_x and L^v_y, are comparable in value and both increase as the rib height increases.

The above analysis of the isopleths of two-point auto-correlations based on figure 24 was conducted at the reference points of different elevations. Indeed, more degrees of freedom are involved in the analysis of a 3-D ribbed duct (in comparison with a 2-D boundary-layer flow), the turbulence structures in the three ribbed ducts of different blockage ratios can be compared from a different angle. Figure 25 compares the 2-D spatial two-point auto-correlation function of streamwise velocity fluctuations at three identical elevations in the central x–y plane ($z/\delta = 0$) for two rib cases of $Br = 0.05$ and 0.2. The comparison of these two ribbed duct cases is made at three identical reference points, with the relative streamwise coordinate fixed at $x'_{ref}/\delta = 0.4$, while the vertical coordinate being $y_{ref}/\delta = -0.4$, 0 and 0.5. A non-trivial value of the inclination angle α (as shown in figure 25) is a reflection of the near-wall ejection events. From figure 25, it is seen that the inclination angle α is negatively valued on the smooth top wall side (at $y_{ref}/\delta = 0.5$). This is simply because the normal direction of the smooth top wall is pointing downwards and, therefore, ejection events near the smooth top wall are associated with downwash flows towards the ribbed bottom wall. By comparing figure 25(*a–c*) with 25(*d–f*), respectively, it is clear that the inclination angle α of the isopleths of R^S_{uu} increases monotonically as the Br value increases from 0.05 to 0.2, resulting in an enhanced flow interaction

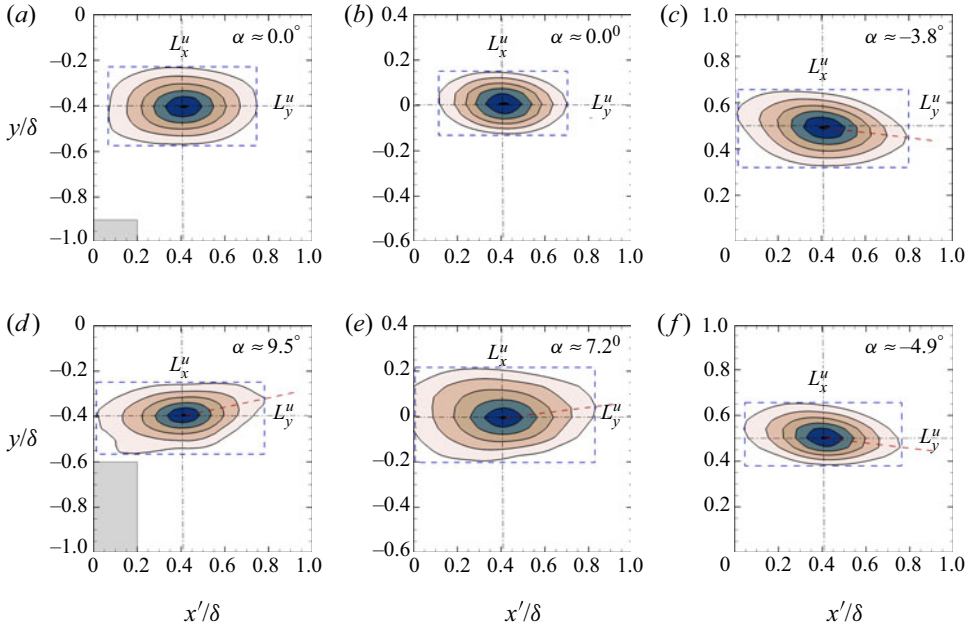

FIGURE 25. Isopleths of streamwise two-point auto-correlation $R^s_{uu}(x'/\delta, y/\delta)$ calculated at three reference points of different elevations in the central vertical plane located at $z/\delta = 0$. The comparison of the two ribbed flow cases (of $Br = 0.05$ and 0.2) is conducted at three identical reference points, with the relative streamwise coordinate fixed at $x'_{ref}/\delta = 0.4$, while the vertical coordinate being $y_{ref}/\delta = -0.4$, 0 and 0.5. The isopleth value ranges from 0.5 to 1.0, with the outermost and innermost isopleths corresponding to $R^s_{uu} = 0.5$ and 1.0, respectively. The increment between two adjacent isopleths is 0.1 for the two rib cases. The dashed box contains exactly the outermost isopleth, with side lengths of L^u_x and L^u_y. (*a*) $Br = 0.05$ at $y_{ref}/\delta = -0.4$, (*b*) $Br = 0.05$ at $y_{ref}/\delta = 0.0$, (*c*) $Br = 0.05$ at $y_{ref}/\delta = 0.5$, (*d*) $Br = 0.2$ at $y_{ref}/\delta = -0.4$, (*e*) $Br = 0.2$ at $y_{ref}/\delta = 0.0$ and (*f*) $Br = 0.2$ at $y_{ref}/\delta = 0.5$.

between the ribbed bottom wall and smooth top wall. Furthermore, from figures 25(*a*) and 25(*d*), it appears that the length scales of turbulence structures are comparable in both the streamwise and vertical directions, indicating that the rib effect on the size of turbulence structures is reduced considerably at an elevation well above the ribs.

Besides the spatial scales of turbulence structures analysed above, the temporal scales of turbulent motions can also be investigated by using the temporal auto-correlation function of velocity fluctuations, defined as

$$R^t_{ij}(t) = \frac{\langle u'_i(t) u'_j(t_{ref})\rangle}{\sqrt{\langle u'^2_i\rangle \langle u'^2_j\rangle}}, \tag{4.2}$$

where t_{ref} represents the reference time origin and superscript 't' denotes a temporal correlation. In figure 26 the temporal auto-correlations of all three velocity components for different rib cases are compared at the elevation that is slightly above the rib crest. The spatial reference points used here are the same as in figure 24 for the calculation of the spatial two-point auto-correlations. From figure 26, it is evident that in all three cases, the temporal integral scale (as indicated by the intercept of time axis) of the streamwise velocity is longer than those of the other two components. This characteristic of the

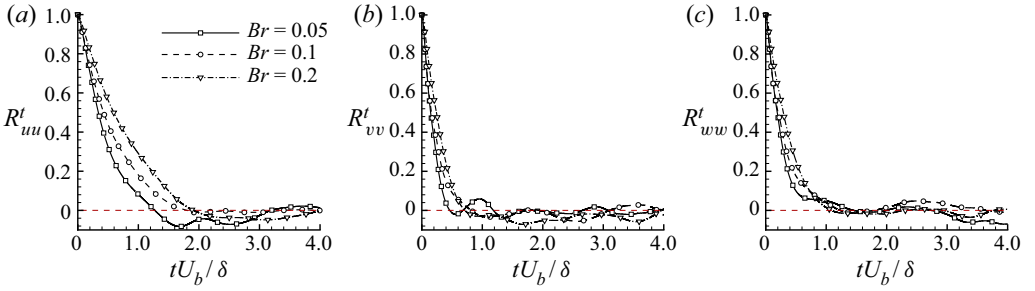

FIGURE 26. Temporal auto-correlations of velocity fluctuations for different blockage ratios at the elevation that is slightly above the rib crest (the spatial reference point is identical to that used in figure 24). (*a*) Profiles of R^t_{uu}, (*b*) profiles of R^t_{vv} and (*c*) profiles of R^t_{ww}.

temporal scale of turbulent flow structures is consistent with the previous analysis of figure 24 in the sense that the largest scale of turbulence structures is associated with the streamwise velocity fluctuations. Both spatial and temporal auto-correlations shown in figures 24 and 26 clearly indicate that turbulence length scales become larger in the region immediately above the rib crest as the rib height increases.

The effects of rib height on the temporal scales of turbulent flow structures can be further quantified using the premultiplied energy spectra ($f E_{ii}/\langle u'u'\rangle$). Figure 27 compares the premultiplied energy spectra of all three components of velocity fluctuations. From figure 27(*a–c*), it is observed that the characteristic temporal scale of turbulence structures increases as the rib height increases, an observation that is consistent with the previous analysis of figures 24 and 26. For example, the mode of $f E_{ii}/\langle u'u'\rangle$ occurs at the non-dimensional temporal scale of $tU_b/\delta \approx 2.77$ in the case of $Br = 0.05$, but at $tU_b/\delta \approx 3.12$ and 4.82 in the cases of $Br = 0.1$ and 0.2, respectively. The properties of these characteristic temporal scales can be further understood by defining the energy-containing range based on the temporal scales possessing premultiplied energy spectra that are at least 70 % of the peak value (bounded by the vertical dashed lines 'P_1' and 'P_2' in figure 27). By comparing figure 27(*a–c*), it is evident that owing to the substantial changes in the temporal scales induced by the rib elements, the difference between the lower (P_1) and upper (P_2) temporal thresholds increases monotonically from $4.0\delta/U_b$ to $5.6\delta/U_b$ as the blockage ratio increases from $Br = 0.05$ to 0.2. This clearly indicates that not only the mode but also the range of the temporal scales of energetic turbulent motions progressively increase as the rib height increases.

4.2. *Turbulence structures in the x–z plane*

As dominant flow structures in near-wall turbulence, streaks play a significant role in the transport of momentum and TKE, and have been well studied in the context of 2-D turbulent boundary layers developed over flat plates (see, e.g. Chernyshenko & Baig 2005; Adrian 2007). In the current test case of 3-D turbulent flow in a ribbed duct, the streamwise streaky structures exhibit interesting features that are qualitatively different from those in canonical 2-D turbulent boundary layers. In particular, the streak structures in a ribbed duct are sensitive to not only the rib height but also the boundary layers developed over the two vertical sidewalls of the duct. To demonstrate the rib height effects on the development of streaky structures, contours of the non-dimensionalized instantaneous streamwise velocity fluctuations, u'/U_b, are plotted in figure 28 in the x–z plane located at $y/\delta = -0.86$, -0.76 and -0.56 for $Br = 0.05$, 0.1 and 0.2, respectively. As shown

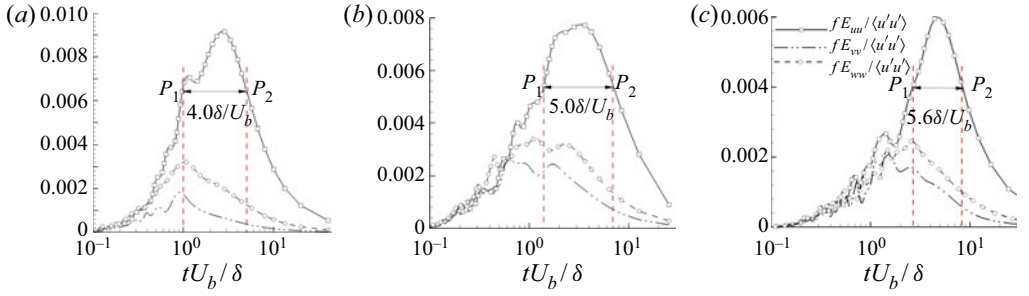

FIGURE 27. Comparison of the premultiplied energy spectra, $fE_{ii}/\langle u'u'\rangle$, of the three components of velocity fluctuations for different blockage ratios at the elevation that is slightly above the rib crest (the spatial reference point is identical to that used in figure 24). (*a*) $Br = 0.05$, (*b*) $Br = 0.1$ and (*c*) $Br = 0.2$.

previously in figures 13 and 15, at these elevations, both the Reynolds stresses and TKE production rate peak. From figure 28(*a–c*), it is seen that both the characteristic length scales and the strengths of low- and high-speed streaks are influenced apparently by the rib height. From the previous analysis (figures 12, 13 and 15), it is understood that as the rib height increases, the magnitudes of both turbulence intensity and TKE production rate increase near the rib crest. Correspondingly, the induced turbulence perturbations by rib elements enhance, leading to an increased streak strength immediately above the rib crest. Clearly, as Br increases from 0.05 to 0.2, the size of the streaky structures increases and, furthermore, the spanwise spacing between neighbouring low- and high-speed streaks also increases. An enhanced strength of streaky structures in the region immediately above the ribs is consistent with our previous observation of reduced turbulent anisotropy detailed in § 3.6. In the following, the rib height effect on the spanwise separation between the streaks will be further investigated using spatial two-point auto-correlation coefficients.

Figure 29 shows the isopleths of the 2-D two-point auto-correlation of streamwise velocity fluctuations in the x–z plane of different elevations for three rib cases. The results are obtained at the same reference points as in figure 24. The spanwise characteristic size of the streaks is denoted as l in the figure, which is represented by the spanwise separation between two outermost isopleths (for $R^s_{uu} = 0.1$) across the reference point. From figure 29(*a–c*), it is clear that the value of l increases monotonically as the rib height increases. Specifically, at the reference point (which is slightly above the rib crest), the spanwise characteristic scale of streaks is approximately one-eighth and one-sixth of the duct width (i.e. $l = D/8$ and $D/6$) for $Br = 0.05$ and 0.1, respectively. However, as Br increases to 0.2, the value of l increases significantly to approximately one-fourth of the duct width (i.e. $l = D/4$). This well explains the qualitative results shown previously in figure 28 that the elongated streaks tend to be stretched in the spanwise direction and be intensified with an increasing rib height.

To refine the study, figure 30 compares the one-dimensional (1-D) spanwise profiles of the two-point auto-correlation coefficients of the three velocity components (R^s_{uu}, R^s_{vv} and R^s_{ww}) for the three rib cases. Given the finite size of the spanwise domain of the duct (bounded by two vertical sidewalls), the value of R^s_{ii} does not vanish at $z/\delta = 1.0$, a feature that is drastically different from that of a canonical 2-D plane-channel flow of an infinite spanwise domain size. The spanwise characteristic length scale of streaks can be defined based on either the 2-D contours of R^s_{uu} shown in figure 29 or the 1-D profile of R^s_{uu} shown in figure 30(*a*). The spanwise separation between the low- and high-speed streaks can be determined precisely based on the position of the negatively valued peak of R^s_{uu}

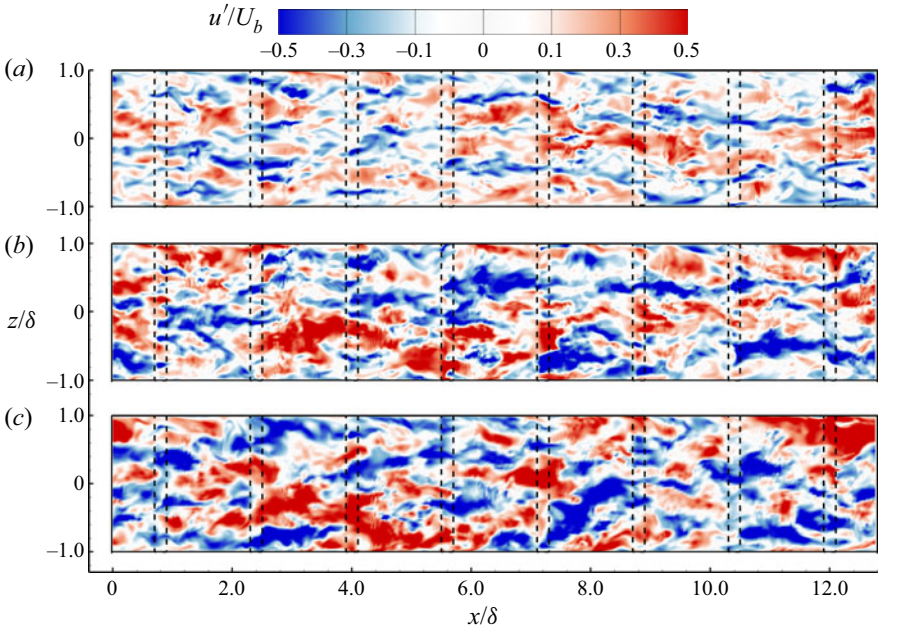

FIGURE 28. Contours of the non-dimensionalized instantaneous streamwise velocity fluctuations u'/U_b in the x–z plane of different elevations immediately above the rib crest for three rib cases. (*a*) $y/\delta = -0.86$ and $Br = 0.05$, (*b*) $y/\delta = -0.76$ and $Br = 0.1$, and (*c*) $y/\delta = -0.56$ and $Br = 0.2$.

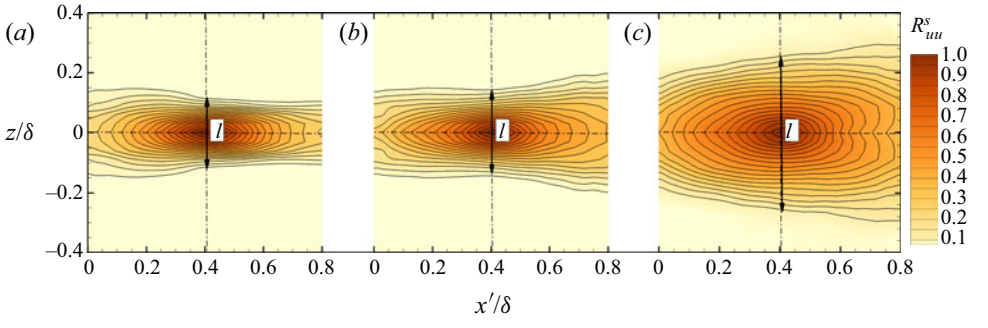

FIGURE 29. Contours of the spatial two-point auto-correlation of streamwise velocity fluctuations R^s_{uu} in the x–z plane for different blockage ratios. The reference point is located in the central vertical plane at $x'_{ref}/\delta = 0.4$ and $z/\delta = 0$, as in figure 24. The isopleth value of R^s_{uu} ranges within [0.1, 1.0], with an increment of 0.05 between two adjacent isopleths. The characteristic spanwise size of the streaks is denoted as l, which is represented by the spanwise separation between two outmost isopleths across the reference point. (*a*) $y/\delta = -0.86$ and $Br = 0.05$, (*b*) $y/\delta = -0.76$ and $Br = 0.1$, and (*c*) $y/\delta = -0.56$ and $Br = 0.2$.

in figure 30(*a*), which is commonly used for evaluating the spanwise characteristic length scale of streaks. From figure 30(*a*), it is evident that the decaying rate of R^s_{uu} becomes increasingly slower as the rib height increases. Consequently, the spanwise characteristic size of the streaky structures (as represented by the spanwise separation between the low- and high-speed streaks) increases monotonically from $z/\delta = 0.2$ to 0.6 as the blockage

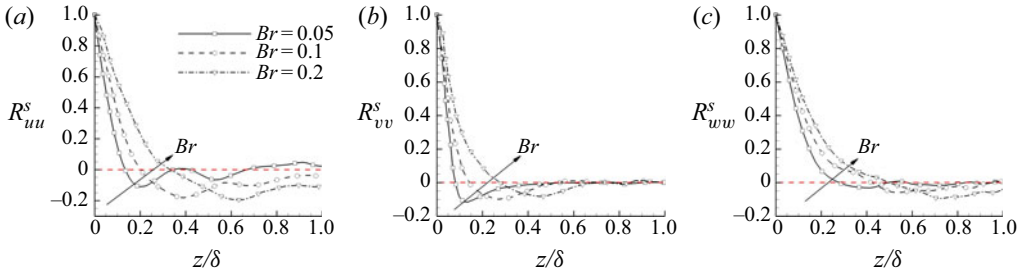

FIGURE 30. Spanwise profiles of the spatial two-point auto-correlations for three different rib cases. The reference point is located in the central vertical plane at $z_{ref}/\delta = 0$ and $x'_{ref}/\delta = 0.4$, and the value of y_{ref}/δ is identical to that in figure 24. (*a*) Profiles of R^s_{uu}, (*b*) profiles of R^s_{vv} and (*c*) profiles of R^s_{ww}.

ratio increases from $Br = 0.05$ to 0.2. As such, the average spanwise streak spacing at $Br = 0.2$ is approximately three and two times larger than those at $Br = 0.05$ and 0.1, respectively. Furthermore, it is observed that the magnitude of R^s_{uu} corresponding to the characteristic spanwise scale of the streaks also increases slightly with an increasing rib height, indicating a monotonic increase in the streaky structure strength above the rib elements, a conclusion that is consistent with qualitative results shown in figure 28. The mode corresponding to the negative peak of R^s_{vv} indicates the diameter of streamwise vortices (streaks). Figure 30(*b*) shows that near the rib crest, the mean diameter of the streamwise streaks increases monotonically; and consequently, the negative peak in the profile of R^s_{vv} shifts from $z/\delta \approx 0.12$ to 0.44 as the rib height increases from $Br = 0.05$ to 0.2. This leads to an interesting conclusion that the mean diameter of streamwise streaks is comparable to the height of the rib elements (which is $H/\delta = 0.1$ and 0.4 for $Br = 0.05$ and 0.2, respectively). By comparing figure 30(*c*) with 30(*a*), it is clear that the profiles of R^s_{ww} are similar to those of R^s_{uu}, both indicating that the spanwise characteristic scale of streaks increases monotonically as the rib height increases. In view of this, it can be concluded that the scales of streamwise streaks, in terms of their width and diameter, increase with an increasing rib height.

5. Conclusions

Direct numerical simulations of fully developed turbulent flow through ribbed square ducts are performed to investigate the effects of rib height on the statistical moments of the velocity field, secondary flow motions and turbulence structures. The pitch-to-height ratios of the three rib cases under the investigation are $P/H = 16$, 8 and 4 (for $Br = 0.05$, 0.1 and 0.2, respectively). In order to identify the rib effects on the velocity field, an additional DNS of a smooth duct flow is conducted at the same Reynolds number of $Re_b = 5600$, which is used as a baseline comparison case in our study. The turbulence field and flow structures of the rib cases are influenced by not only the aspect ratio of the ribs but also the four sidewalls of the duct. A ribbed duct flow is intrinsically 3-D and statistically inhomogeneous in all three directions, which is qualitatively different from the classical case of a 2-D rough-wall boundary-layer flow.

The mean flow patterns of cases of $Br = 0.05$ and 0.1 are typical of *k*-type rough-wall flows, but that of $Br = 0.2$ exhibits features that are characteristic of a *d*-type rough-wall flow. Furthermore, under the 3-D flow conditions, organized secondary flows appear in the cross-stream directions whose strength decreases monotonically near the bottom corner of

the ducts but increases monotonically near the side and top walls as the blockage ratio increases. The spatial distributions of the local skin friction coefficient C_f and pressure coefficient C_p are influenced significantly by the complex geometry of the domain and the secondary flow pattern in the cross-stream directions. The values of both C_f and C_p maintain approximately constant in the spanwise direction in the central region of the duct. In the streamwise direction, however, the highest value of C_f occurs around the leeward and windward faces of the ribs corresponding to the cores of the recirculation bubble and upstream vortex, respectively. The magnitude of C_p is the highest near the windward face of the ribs, and increases as the rib height increases as a result of an enhanced impinging effect of the flow.

Characteristic of a smooth duct flow, the profiles of the Reynolds normal and shear stresses are symmetrical and anti-symmetrical about the duct centre ($y/\delta = 0$), respectively. By contrast, the profiles of all Reynolds stress components are asymmetrical in the three rib cases due to the presence of ribs. In general, the magnitudes of the Reynolds normal and shear stresses of the ribbed duct flows are much larger than those of the smooth duct flow due to the disturbances from the ribs. The magnitudes of Reynolds shear stresses and TKE enhance as the rib height increases. For all three rib cases, the highest Reynolds stress levels occur slightly above the rib crest, where the shear effect is the greatest. For the three rib cases tested, the magnitude of $\langle u'u' \rangle$ is much larger than those of $\langle v'v' \rangle$ and $\langle w'w' \rangle$, making the largest contribution to the value of TKE among the three Reynolds normal stress components. Owing to the cross-stream secondary flow motions, the profile of $-\langle u'v' \rangle$ peaks in the region between the sidewall and duct centre. In fact, the turbulence level as indicated by the magnitudes of Reynolds normal and shear stresses all increase monotonically as the rib height increases in the central region of the duct.

The maximum value of the TKE production rate over the dissipation rate P_k/ε_k occurs immediately above the rib crest and in the region between the sidewall and duct centre, creating a zone of strong non-equilibrium turbulence. In the streamwise-vertical directions, high-intensity vortices are generated at the leading edge of the ribs, which then shed into the central core region of the duct. Concurrently, in the spanwise-vertical directions, secondary flow motions carry these highly energetic vortices from the duct centre sideways to the two vertical walls, resulting in an increase in the value of P_k/ε_k. The transport equation of TKE is studied to further understand the rib effects on turbulence energy transfer. The budget balances of the three rib cases exhibit more complex patterns than that of the smooth duct flow, especially around the rib crest. In comparison with the smooth duct flow, the dominant source term is still the production term P_k, which peaks at a position that is slightly above rib crest in all three rib cases. Although the magnitudes of the three sinks (D_k, T_k and ε) around the rib crest are comparable at $Br = 0.05$, the turbulent diffusion term T_k becomes increasingly dominant as the blockage ratio increases to $Br = 0.1$ and 0.2. The convection term C_k does not make a remarkable contribution to the budget balance of TKE in a smooth duct flow. By contrast, the effect of the convection term C_k becomes more pronounced due to the complex mean flow pattern and high TKE level around the rib crest in all three rib cases.

The study of turbulence anisotropy at both large- and small-scales indicates that the degree of turbulence anisotropy is sensitive to the rib height. In the region between the rib crest and the smooth top wall, there is a clear indication of turbulence anisotropy based on the study of the anisotropy tensors of the Reynolds normal stresses and dissipation rates, b_{ii} and d_{ii}, respectively. This is because the magnitude of b_{11} is larger than those of b_{22} and b_{33}; and similarly, the magnitude of d_{11} is greater than those of d_{22} and d_{33} in this region. Furthermore, it is interesting to observe that as the blockage ratio increases from

$Br = 0.05$ to 0.2, the peak values of the dominant streamwise components, b_{11} and d_{11}, decrease monotonically near the rib crest. This is because the disturbances from the ribs become stronger as the rib height increases, which facilitates distribution of TKE to all three directions, therefore reducing the degree of turbulence anisotropy. It is interesting to observe that the magnitudes of the normal components of the dissipation anisotropy tensor, d_{11}, d_{22} and d_{33}, are close to zero in the duct centre for $-0.5 < y/\delta < 0.5$. This indicates that small-scale structures exhibit a stronger 'return to isotropy' tendency compared to the large-scale structures in the duct centre.

The turbulent flow structures are further studied using the JPDF of the streamwise and vertical velocity fluctuations, λ_{ci}-criterion, temporal auto-correlations, temporal spectra and spatial two-point auto-correlations of the turbulence field. The results show that an increase of the rib height exerts stronger disturbances to the flow field, which are subsequently deflected to the duct centre. This phenomenon leads to the formation of incoherent structures and the generation of violent ejection and sweep motions just above the rib elements, giving rise to an increase of the local TKE production rate. Based on the analysis of the 2-D spatial two-point auto-correlation function of velocity fluctuations, it is discovered that in the region slightly above the rib crest, the inclination angle of the isopleths of R^s_{uu} decreases monotonically from $\alpha = 12.5^\circ$ to 8.0° as the blockage ratio increases from $Br = 0.05$ to 0.2. This monotonic trend with respect to Br is also evident from the JPDF analysis, which shows that the turbulent flow becomes increasingly dominated by the sweep events near the rib crest; and as a result, a lower magnitude of the inclination angle is observed around the rib height. However, based on the analysis of R^s_{uu} of different rib cases at the same elevation, it is observed that the inclination angle α increases monotonically as the Br value increases at an elevation well above the ribs, resulting in an enhanced flow interaction between the ribbed bottom wall and the smooth top wall. It is interesting to observe that both temporal and spatial characteristic scales of turbulence increase monotonically as the rib height increases around the rib crest. Furthermore, based on an analysis of the non-dimensionalized streamwise premultiplied temporal spectrum $fE_{ii}/\langle u'u'\rangle$ of velocity fluctuations, it is observed that the range of temporal scales of the most energetic turbulence motions (with the value of $fE_{ii}/\langle u'u'\rangle$ being at least 70 % of its peak value) also expands monotonically around the rib height as the rib height increases. In addition, both the spanwise characteristic size of the streaks and the diameter of streamwise vortices increase monotonically as the rib height increases. More specifically, the non-dimensional diameter of streamwise vortices increases from $z/\delta = 0.12$ to 0.44 as the blockage ratio increases from $Br = 0.05$ to 0.2, comparable in value to the height of the rib elements (i.e. $H/\delta = 0.1$ and 0.4 for $Br = 0.05$ and 0.2, respectively).

Acknowledgements

The authors would like to thank Western Canada Research Grid (WestGrid) for access to supercomputing and storage facilities. Research funding from the Natural Sciences and Engineering Research Council (NSERC) of Canada to B.-C.W. is gratefully acknowledged.

Declaration of interests

The authors report no conflict of interest.

REFERENCES

ADRIAN, R. J. 2007 Hairpin vortex organization in wall turbulence. *Phys. Fluids* **19**, 041301.

ADRIAN, R. J., MEINHART, C. D. & TOMKINS, C. D. 2000 Vortex organization in the outer region of the turbulent boundary layer. *J. Fluid Mech.* **422**, 1–54.

ANDREOPOULOS, J. & BRADSHAW, P. 1981 Measurements of turbulence structure in the boundary layer on a rough surface. *Boundary-Layer Meteorol.* **20**, 201–213.

BANDYOPADHYAY, P. R. 1987 Rough-wall turbulent boundary layers in the transition regime. *J. Fluid Mech.* **180**, 231–266.

BHAGANAGAR, K. 2008 Direct numerical simulation of unsteady flow in channel with rough walls. *Phys. Fluids* **20**, 101508.

BHAGANAGAR, K. & CHAU, L. 2015 Characterizing turbulent flow over 3-D idealized and irregular rough surfaces at low Reynolds number. *Appl. Math. Model.* **39**, 6751–6766.

BHAGANAGAR, K., KIM, J. & COLEMAN, G. 2004 Effect of roughness on wall-bounded turbulence. *Flow Turbul. Combust.* **72**, 463–492.

BORELLO, D., SALVAGNI, A. & HANJALIĆ, K. 2015 Effects of rotation on flow in an asymmetric rib-roughened duct: LES study. *Intl J. Heat Fluid Flow* **55**, 104–119.

BURATTINI, P., LEONARDI, S., ORLANDI, P. & ANTONIA, R. A. 2008 Comparison between experiments and direct numerical simulations in a channel flow with roughness on one wall. *J. Fluid Mech.* **600**, 403–426.

CASARSA, L. & ARTS, T. 2005 Experimental investigation of the aerothermal performance of a high blockage rib-roughened cooling channel. *Trans. ASME: J. Turbomach* **127**, 580–588.

CHAN, L., MACDONALD, M., CHUNG, D., HUTCHINS, N. & OOI, A. 2015 A systematic investigation of roughness height and wavelength in turbulent pipe flow in the transitionally rough regime. *J. Fluid Mech.* **771**, 743–777.

CHERNYSHENKO, S. I. & BAIG, M. F. 2005 The mechanism of streak formation in near-wall turbulence. *J. Fluid Mech.* **544**, 99–131.

CHOI, H., MOIN, P. & KIM, J. 1993 Direct numerical simulation of turbulent flow over riblets. *J. Fluid Mech.* **255**, 503–539.

CHRISTENSEN, K. T. & ADRIAN, R. J. 2001 Statistical evidence of hairpin vortex packets in wall turbulence. *J. Fluid Mech.* **431**, 433–443.

COCEAL, O., DOBRE, A., THOMAS, T. G. & BELCHER, S. E. 2007 Structure of turbulent flow over regular arrays of cubical roughness. *J. Fluid Mech.* **589**, 375–409.

COLETTI, F., CRESCI, I. & ARTS, T. 2013 Spatio-temporal analysis of the turbulent flow in a ribbed channel. *Intl J. Heat Fluid Flow* **44**, 181–196.

COLETTI, F., LO JACONO, D., CRESCI, I. & ARTS, T. 2014 Turbulent flow in rib-roughened channel under the effect of Coriolis and rotational buoyancy forces. *Phys. Fluids* **26**, 045111.

COLETTI, F., MAURER, T., ARTS, T. & DI SANTE, A. 2012 Flow field investigation in rotating rib-roughened channel by means of particle image velocimetry. *Exp. Fluids* **52**, 1043–1061.

FANG, X., YANG, Z., WANG, B. C., TACHIE, M. F. & BERGSTROM, D. J. 2015 Highly-disturbed turbulent flow in a square channel with V-shaped ribs on one wall. *Intl J. Heat Fluid Flow* **56**, 182–197.

FANG, X., YANG, Z., WANG, B.-C., TACHIE, M. F. & BERGSTROM, D. J. 2017 Large-eddy simulation of turbulent flow and structures in a square duct roughened with perpendicular and V-shaped ribs. *Phys. Fluids* **29**, 065110.

GAVRILAKIS, S. 1992 Numerical simulation of low-Reynolds-number turbulent flow through a straight square duct. *J. Fluid Mech.* **244**, 101–129.

GRIFFITH, B. E. & PATANKAR, N. A. 2020 Immersed methods for fluid–structure interaction. *Annu. Rev. Fluid Mech.* **52**, 421.

HAN, J. C., DUTTA, S. & EKKAD, S. 2012 *Gas Turbine Heat Transfer and Cooling Technology*. CRC.

HIROTA, M., YOKOSAWA, H. & FUJITA, H. 1992 Turbulence kinetic energy in turbulent flows through square ducts with rib-roughened walls. *Intl J. Heat Fluid Flow* **13**, 22–29.

HURTHER, D., LEMMIN, U. & TERRAY, E. A. 2007 Turbulent transport in the outer region of rough-wall open-channel flows: the contribution of large coherent shear stress structures (LC3S). *J. Fluid Mech.* **574**, 465–493.

IKEDA, T. & DURBIN, P. A. 2007 Direct simulations of a rough-wall channel flow. *J. Fluid Mech.* **571**, 235–263.

ISMAIL, U., ZAKI, T. A. & DURBIN, P. A. 2018 Simulations of rib-roughened rough-to-smooth turbulent channel flows. *J. Fluid Mech.* **843**, 419–449.

JACKSON, P. S. 1981 On the displacement height in the logarithmic velocity profile. *J. Fluid Mech.* **111**, 15–25.

KEIRSBULCK, L., LABRAGA, L., MAZOUZ, A. & TOURNIER, C. 2002 Surface roughness effects on turbulent boundary layer structures. *Trans. ASME: J. Fluids Engng* **124**, 127–135.

KIM, J., MOIN, P. & MOSER, R. 1987 Turbulence statistics in fully developed channel flow at low Reynolds number. *J. Fluid Mech.* **177**, 133–166.

KROGSTAD, P.-Å., ANDERSSON, H. I., BAKKEN, O. M. & ASHRAFIAN, A. 2005 An experimental and numerical study of channel flow with rough walls. *J. Fluid Mech.* **530**, 327–352.

KROGSTAD, P.-Å. & ANTONIA, R. A. 1994 Structure of turbulent boundary layers on smooth and rough walls. *J. Fluid Mech.* **277**, 1–21.

KROGSTAD, P.-Å. & ANTONIA, R. A. 1999 Surface roughness effects in turbulent boundary layers. *Exp. Fluids* **27**, 450–460.

LABBÉ, O. 2013 Large-eddy-simulation of flow and heat transfer in a ribbed duct. *Comput. Fluids* **76**, 23–32.

LAMBALLAIS, E., LESIEUR, M. & MÉTAIS, O. 1997 Probability distribution functions and coherent structures in a turbulent channel. *Phys. Rev.* E **56**, 6761–6766.

LEE, J. H., SUNG, H. J. & KROGSTAD, P.-Å. 2011 Direct numerical simulation of the turbulent boundary layer over a cube-roughened wall. *J. Fluid Mech.* **669**, 397–431.

LEONARDI, S. & CASTRO, I. P. 2010 Channel flow over large cube roughness: a direct numerical simulation study. *J. Fluid Mech.* **651**, 519–539.

LEONARDI, S., ORLANDI, P., DJENIDI, L. & ANTONIA, R. A. 2004 Structure of turbulent channel flow with square bars on one wall. *Intl J. Heat Fluid Flow* **25**, 384–392.

LEONARDI, S., ORLANDI, P., SMALLEY, R. J., DJENIDI, L. & ANTONIA, R. A. 2003 Direct numerical simulations of turbulent channel flow with transverse square bars on one wall. *J. Fluid Mech.* **491**, 229–238.

LIOU, T. M., WU, Y. Y. & CHANG, Y. 1993 LDV measurements of periodic fully developed main and secondary flows in a channel with rib-disturbed walls. *Trans. ASME: J. Fluids Engng* **115**, 109–114.

LIU, Y. Z., KE, F. & SUNG, H. J. 2008 Unsteady separated and reattaching turbulent flow over a two-dimensional square rib. *J. Fluids Struct.* **24**, 366–381.

LOHÁSZ, M. M., RAMBAUD, P. & BENOCCI, C. 2006 Flow features in a fully developed ribbed duct flow as a result of miles. *Flow Turbul. Combust.* **77**, 59–76.

MACDONALD, M., CHAN, L., CHUNG, D., HUTCHINS, N. & OOI, A. 2016 Turbulent flow over transitionally rough surfaces with varying roughness densities. *J. Fluid Mech.* **763**, 130–161.

MAZOUZ, A., LABRAGA, L. & TOURNIER, C. 1998 Anisotropy invariants of Reynolds stress tensor in a duct flow and turbulent boundary layer. *Trans. ASME: J. Fluids Engng* **120**, 280–284.

MITTAL, R. & IACCARINO, G. 2005 Immersed boundary methods. *Annu. Rev. Fluid Mech.* **37**, 239–261.

MOMPEAN, G., GAVRILAKIS, S., MACHIELS, L. & DEVILLE, M. O. 1996 On predicting the turbulence-induced secondary flows using nonlinear k-ε models. *Phys. Fluids* **8**, 1856–1868.

MOSER, R. D. & MOIN, P. 1987 The effects of curvature in wall-bounded turbulent flows. *J. Fluid Mech.* **175**, 479–510.

NAGANO, Y., HATTORI, H. & HOURA, T. 2004 DNS of velocity and thermal fields in turbulent channel flow with transverse-rib roughness. *Intl J. Heat Fluid Flow* **25**, 393–403.

NOORMOHAMMADI, A. & WANG, B.-C. 2019 DNS study of passive plume interference emitting from two parallel line sources in a turbulent channel flow. *Intl J. Heat Fluid Flow* **77**, 202–216.

ORLANDI, P., LENOARDI, S. & ANTONIA, R. A. 2006 Turbulent channel flow with either transverse or longitudinal roughness elements on one wall. *J. Fluid Mech.* **561**, 279–305.

PERRY, A. E., SCHOFIELD, W. H. & JOUBERT, P. N. 1969 Rough wall turbulent boundary layers. *J. Fluid Mech.* **37**, 383–413.

PESKIN, C. S. 1972 Flow patterns around heart valves: a numerical method. *J. Comput. Phys.* **10**, 252–271.

PHILIPS, D. A., ROSSI, R. & IACCARINO, G. 2013 Large-eddy simulation of passive scalar dispersion in an urban-like canopy. *J. Fluid Mech.* **723**, 404–428.

PINELLI, A., NAQAVI, I. Z., PIOMELLI, U. & FAVIER, J. 2010*a* Immersed-boundary methods for general finite-difference and finite-volume Navier–Stokes solvers. *J. Comput. Phys.* **229**, 9073–9091.

PINELLI, A., UHLMANN, M., SEKIMOTO, A. & KAWAHARA, G. 2010*b* Reynolds number dependence of mean flow structure in square duct turbulence. *J. Fluid Mech.* **644**, 107–122.

PIROZZOLI, S., MODESTI, D., ORLANDI, P. & GRASSO, F. 2018 Turbulence and secondary motions in square duct flow. *J. Fluid Mech.* **840**, 631–655.

POPE, S. B. 2000 *Turbulent Flows*. Cambridge University Press.

ROUHI, A., CHUNG, D. & HUTCHINS, N. 2019 Direct numerical simulation of open-channel flow over smooth-to-rough and rough-to-smooth step changes. *J. Fluid Mech.* **866**, 450–486.

SCOTTI, A. 2006 Direct numerical simulation of turbulent channel flows with boundary roughened with virtual sandpaper. *Phys. Fluids* **18**, 031701.

SEWALL, E. A., TAFTI, D. K., GRAHAM, A. B. & THOLE, K. A. 2006 Experimental validation of large eddy simulations of flow and heat transfer in a stationary ribbed duct. *Intl J. Heat Fluid Flow* **27**, 243–258.

SHAFI, H. S. & ANTONIA, R. A. 1997 Small-scale characteristics of a turbulent boundary layer over a rough wall. *J. Fluid Mech.* **342**, 263–293.

SHISHKINA, O. & WAGNER, C. 2011 Modelling the influence of wall roughness on heat transfer in thermal convection. *J. Fluid Mech.* **686**, 568–582.

SPEZIALE, C. G. & GATSKI, T. B. 1997 Analysis and modelling of anisotropies in the dissipation rate of turbulence. *J. Fluid Mech.* **344**, 155–180.

THOM, A. S. 1971 Momentum absorption by vegetation. *Q. J. R. Meteorol. Soc.* **97**, 414–428.

TOWNSEND, A. A. R. 1980 *The Structure of Turbulent Shear Flow*. Cambridge University Press.

VINUESA, R., NOORANI, A., LOZANO-DURÁN, A., KHOURY, G. K. E., SCHLATTER, P., FISCHER, P. F. & NAGIB, H. M. 2014 Aspect ratio effects in turbulent duct flows studied through direct numerical simulation. *J. Turbul.* **15**, 677–706.

VOLINO, R. J., SCHULTZ, M. P. & FLACK, K. A. 2009 Turbulence structure in a boundary layer with two-dimensional roughness. *J. Fluid Mech.* **635**, 75–101.

WAGNER, S. & SHISHKINA, O. 2015 Heat flux enhancement by regular surface roughness in turbulent thermal convection. *J. Fluid Mech.* **763**, 109–135.

WANG, L., HEJCIK, J. & SUNDEN, B. 2007 PIV measurement of separated flow in a square channel with streamwise periodic ribs on one wall. *Trans. ASME: J. Fluids Engng* **129**, 834–841.

WANG, L., SALEWSKI, M. & SUNDÉN, B. 2010 Turbulent flow in a ribbed channel: flow structures in the vicinity of a rib. *Exp. Therm. Fluid Sci.* **34**, 165–176.

WANG, L. & SUNDÉN, B. 2005 Experimental investigation of local heat transfer in a square duct with continuous and truncated ribs. *Exp. Heat Trans.* **18**, 179–197.

XUN, Q.-Q. & WANG, B.-C. 2016 Hybrid RANS/LES of turbulent flow in a rotating rib-roughened channel. *Phys. Fluids* **28**, 075101.

YAGLOM, A. M. & KADER, B. A. 1974 Heat and mass transfer between a rough wall and turbulent fluid flow at high Reynolds and peclet numbers. *J. Fluid Mech.* **62**, 601–623.

YANG, D. & SHEN, L. 2010 Direct-simulation-based study of turbulent flow over various waving boundaries. *J. Fluid Mech.* **650**, 131–180.

YOKOSAWA, H., FUJITA, H., HIROTA, M. & IWATA, S. 1989 Measurement of turbulent flow in a square duct with roughened walls on two opposite sides. *Intl J. Heat Fluid Flow* **10**, 125–130.

YUAN, J. & PIOMELLI, U. 2014 Roughness effects on the Reynolds stress budgets in near-wall turbulence. *J. Fluid Mech.* **760**, 1–11.